AGU PUBLICATIONS

JGR

Journal of Geophysical Research: Oceans

RESEARCH ARTICLE

10.1002/2013JC009729

Key Points:
- Wind and wave climate is analyzed by EOFs in the time and frequency domains
- The frequency domain results capture oscillatory climate features
- Dominant frequency components are identified in each basin providing new insight

Supporting Information:
- Readme
- Figure S1
- Figure S2
- Figure S3
- Figure S4
- Figure S5
- Figure S6
- Figure S7
- Figure S8
- Figure S9
- Figure S10
- Figure S11
- Figure S12

Correspondence to:
K. F. Cheung,
cheung@hawaii.edu

Citation:
Stopa, J. E., and K. F. Cheung (2014), Periodicity and patterns of ocean wind and wave climate, *J. Geophys. Res. Oceans*, *119*, 5563–5584, doi:10.1002/2013JC009729.

Received 14 DEC 2013
Accepted 3 AUG 2014
Accepted article online 7 AUG 2014
Published online 28 AUG 2014

Periodicity and patterns of ocean wind and wave climate

Justin E. Stopa[1,2] and Kwok Fai Cheung[1]

[1]Department of Ocean and Resources Engineering, University of Hawaii at Manoa, Honolulu, Hawaii, USA, [2]Now at Laboratoire d'Oceanographie Spatiale, Ifremer, Plouzane, France

Abstract The Climate Forecast System Reanalysis (CFSR) provides a wealth of information spanning 1979–2009 for investigation of ocean wind and wave climate. Preprocessing of the data is necessary to remove the dominant seasonal signals and to create time series of semimonthly averaged wind speed and significant wave height over a 0.5° global grid. We perform an empirical orthogonal function (EOF) analysis to extract the dominant space-time patterns. The results for the three major ocean basins show strong zonal structures in the winds and saturation of the swells corroborating prior works with various data sets. We reexamine the CFSR data in the frequency domain to identify periodic signals associated with published climate indices. The Fourier transform of the preprocessed time series generates spectra ranging from 1 month to 15 years period for an EOF analysis. The results demonstrate the spatial structures and periods of climate phenomena. The Arctic Oscillation dominates the Atlantic basin with a broad range of intra-annual signals off the European coasts. The Indian and Pacific Oceans are strongly influenced by inter-annual cycles of the El Niño Southern Oscillation (ENSO) and the Antarctica Oscillation. The Indian Ocean also has strong intra-annual components ranging from 50 to 80 days period. The ENSO proves to be a ubiquitous signal around the globe, and in particular, saturates the Pacific with strong influences in the equatorial region and the Southern Hemisphere Westerlies. A commonality of all basins is that the magnitude and the spatial structure of the intra-annual and inter-annual signals are similar suggesting a wide range of periods in each of the climate cycles examined.

1. Introduction

Wind-generated waves propagate across the oceans transporting energy that shapes shorelines, influences maritime commerce, and defines coastal land use around the world. Research in ocean wind and wave climate has assumed greater importance with both societal impacts and scientific contributions. The data-driven endeavor requires multidecadal time series with adequate spatial and temporal resolution to describe climate cycles from intra-annual to inter-annual as well as their signatures across open oceans and sheltered seas. High-quality wind and wave observations in excess of 20 years are available for climate research. These include voluntary observations along shipping routes [*Gulev et al*., 2003], point measurements at buoys [e.g., *Bromirski et al*., 2005; *Menendez et al*., 2008; *Gemmrich et al*., 2011], and spatial patterns from altimeters [e.g., *Young*, 1999; *Woolf et al*., 2002; *Chen et al*., 2002; *Hemer et al*., 2010; *Young et al*., 2011]. Some of these studies supplemented the measurements with detailed wave data from numerical models to provide space-time connections of the observed processes.

The National Centers for Environmental Prediction (NCEP) and the European Centre for Medium-Range Weather Forecasts (ECMWF) have recently produced state-of-the-art global data sets known as the Climate Forecast System Reanalysis (CFSR) and the ECMWF Reanalysis Interim (ERA-I) from 1979 to the present time [*Saha et al*., 2010; *Dee et al*., 2011]. While ERA-I includes wave data through a coupled model system, *Chawla et al*. [2013] utilized CFSR surface winds to generate hindcast wave data with WAVEWATCH III of *Tolman et al*. [2002]. *Stopa and Cheung* [2014] showed ERA-I is more consistent through time, while CFSR better resolves the upper percentiles and variability in comparison to buoy and altimetry measurements. Reanalysis wind and wave data sets have advantage over in situ and remotely sensed observations because they resolve multiscale processes by their high spatial and temporal resolution [*Semedo et al*., 2011; *Rascle and Ardhuin*, 2013]. This allows more intricate studies of the climate impacts from extratropical cyclones to nearshore processes [e.g., *Wang et al*., 2006; *Bromirski et al*., 2013]. The 30-plus years of reanalysis data have enabled studies of inter-annual climate cycles [*Fan et al*., 2012; *Stopa et al*., 2013a].

The previous studies link observations or reanalysis data to established climate indices with two general approaches. The first approach uses empirical orthogonal functions (EOFs) to describe space-time variability of the data. The principal components from the dominant modes are related to indices of established climate cycles [*Wang and Swail*, 2001; *Sterl and Caires*, 2005; *Gulev and Grigorieva*, 2006; *Semedo et al.*, 2011]. The second approach correlates the climate indices, which are typically created from an EOF analysis, directly to the wind and wave data [e.g., *Fan et al.*, 2012; *Stopa et al.*, 2013a; *Shimura et al.*, 2013]. The EOFs are common to both approaches and provide a systematic procedure to identify spatial patterns and describe their time evolution. Climate cycles have periodicities that have not been fully explored because the standard techniques in the time domain do not directly resolve them. The Fourier transform offers an alternative approach to analyze time series by partitioning the variance into frequency components in the form of power spectra. Application of EOFs to the power spectra can objectively identify the dominant frequencies and their spatial patterns from a reanalysis data set.

In this paper, we implement a combined Fourier transform and EOF approach to investigate the climate periodicity and patterns of the CFSR wind and wave data sets from *Saha et al*. [2010] and *Chawla et al*. [2013]. The conventional EOF analysis in the time domain provides a baseline for comparison with the frequency domain results and findings from previous studies. Section 2 summarizes the CFSR data sets and the preprocessing of the wind speed and significant wave height, while section 3 outlines the EOF analysis of the spatial data in the time and frequency domains for the climate study. Section 4 presents the published climate indices for validation of the computed signals and the indices calculated from CFSR for assessment of the phenomena within the data sets. Section 5 presents the EOFs and principal components in the time and frequency domains as well as the spectral density distributions at dominant oscillations periods. The results are organized by ocean basins: Atlantic, Indian, and Pacific, to highlight their distinct climate features and followed by a discussion of their teleconnections. Section 6 provides a summary of major findings and concluding remarks. The supporting information contains the results from a parallel analysis of the ERA-I data set to provide an independent view of the climate cycles and patterns for verification.

2. Climate Forecast System Reanalysis and Preprocessing

The Climate Forecast System Reanalysis has evolved from a series of reanalysis projects worldwide. *Saha et al*. [2010] describe the main advancements over its predecessors, Reanalysis I (R1) and Reanalysis II (R2), also developed at NCEP [*Kalnay et al*., 1996; *Kistler et al*., 2001]. These include an interactive sea ice model, assimilation of satellite radiances, increased resolution in the atmospheric model, and most importantly, coupling between the atmosphere, ocean, and land surface models. The Global Forecast System (GFS) of *Yang et al*. [2006] constitutes the atmospheric model, which has ~38 km horizontal resolution and 64 layers extending from the surface to the 0.26 hPa level. The Geophysical Fluid Dynamic Lab's Modular Ocean Model (MOM) version 4 describes the ocean circulation at 0.25–0.5° resolution with 40 levels extending to 4737 m depth. The land model of *Ek et al*. [2003] includes four soil layers and the ice model has two layers to account for variations below the surface. CFSR uses the same models and data assimilation techniques in three space dimensions (3-D-Var) at each initialization of the reanalysis.

Chawla et al. [2013] utilized atmospheric and oceanographic data from CFSR in WAVEWATCH III to reproduce the wave conditions for 1979–2009. The spectral wave model evolves the action density for a range of wave numbers and all directions under wind forcing and geographical constraints. The hindcast utilized the source term package from *Tolman and Chalikov* [1996] to set a baseline for improvement of spectral wave modeling through the NOAA Partnership Program (NOPP) [*Tolman et al*., 2013]. Hourly surface winds at 10 m elevation along with the temperature difference between the ocean and atmosphere from CFSR provided the forcing to WAVEWATCH III. Passive microwave sensors from the Special Sensor Microwave Imager (SSMI) missions were used to define the daily ice concentrations. The hindcast consists of a mosaic of 16 grids with resolution ranging from 1/15° to 1/2°. Subgrid features, like islands and atolls, are accounted for by prorating the energy transfer through a given computational cell in two perpendicular directions [*Chawla and Tolman*, 2008].

Chawla et al. [2013] and *Stopa and Cheung* [2014] have examined and validated the CFSR wind and wave data sets spanning 30 years from 1979 to 2009. Their results show the data sets have excellent agreement to buoy and altimetry measurements within 5–10% errors up to the 99.9th percentile. The data sets contain multiscale processes ranging from diurnal to inter-annual for a variety of applications and studies. Although the improved prediction in the Southern Ocean associated with additional assimilation data beginning 1994 creates a discontinuity in the time series, the artifact is well outside the period range of the climate cycles of interest here. For the present investigation, we focus on basin-wide processes within the 0.5° global grid and create time series of semimonthly averaged wind speed and significant wave height from the original 3 h increments. The approximate 15 day average allows resolution of intra-annual signals and reduces high-frequency noises and computational requirements. The averaging also mitigates the effects of nonhomogeneous positive biases, which exist in the upper percentiles of the CFSR data [*Stopa and Cheung*, 2014].

The wind and wave data sets have strong seasonal signals associated with the annual cycle that would saturate the EOF analysis obscuring the more subtle climate processes. The seasonal signals are removed a priori using a multivariant analysis. Let x_{ij} denote the wind speed or significant wave height at the ith of the M grid points and the jth of the N time steps. A multivariate regression represents the seasonal signals with K frequencies as

$$\hat{x}_{ij} = a_{i0} + \sum_{k=1}^{K} \left[b_{ik} \cos\left(2\pi f_k \Delta t_j\right) + c_{ik} \sin\left(2\pi f_k \Delta t_j\right) \right] \quad 0 \le j \le N, \tag{1}$$

where Δt is the sampling interval and f_k are the discrete frequencies for the annual signals at 1 cycle per year (cpy) and the associated higher harmonics at 2, 3, and 4 cpy having considerable energy above the noise level. The coefficients, a, b, and c, minimize the sum of the squared errors

$$\sum_{j=1}^{N} \varepsilon_{ij}^2 = \sum_{j=1}^{N} \left[x_{ij} - \hat{x}_{ij} \right]^2. \tag{2}$$

The anomaly time series is then constructed by subtracting the seasonal signals $\hat{x}_{ij}$ from the original time series x_{ij}. The resulting semimonthly time series accentuate the climate variability for subsequent analysis.

3. Methodology

The EOF method is an effective technique for analyzing the dominant modes of variability in geophysical data sets. It is typically applied to spatial-temporal data for detection of patterns by energy level. For harmonic signals, it is preferable to implement the method to spatial data in the frequency domain. We utilize the fast Fourier transform to convert the spatial data x_{ij} over time into the spectral density s_{ik} at $N/2$ frequencies indexed by k. The procedure assumes no energy above the Nyquist frequency and repetition of the entire time series. The latter creates energy leakage and the effect is mitigated by preprocessing of the deseasoned time series with the Hanning window. The resulting Fourier coefficients are rescaled to account for energy loss. Implementation of these procedures at all grid points defines the spatial distribution of the spectral density for visualization and analysis of geophysical processes that otherwise would not be obvious in the time domain [e.g., *Munger and Cheung*, 2008; *Roeber et al*., 2010; *Cheung et al*., 2013].

The large wind speed and wave height in the Westerlies might mask the subtle climate signals in the equatorial region. The deseasoned time series x_{ij} at each grid point is normalized by its standard deviation prior to the time domain EOF analysis. In the frequency domain, the normalization can be handled more efficiently through removal of the "red" spectrum from the spectral density s_{ik}. The red spectrum represents the background energy, which can be deduced from autoregression of the time series. Based on *Gilman et al*. [1963], we estimate the red spectrum as

$$\hat{s}_{ik} = r_i \left[\frac{1-\rho_i^2}{1-2\rho_i \cos\left(2k\pi/N\right) + \rho_i^2} \right], \tag{3}$$

where k ranges from 0 to $N/2$, ρ_i is the autocorrelation of x_{ij} and $x_{i(j+1)}$, and r is a scaling factor that equalizes the variance for the given location. The total variance is conserved by scaling r against the spectral density as

$$r_i = \sum_{k=1}^{N/2} s_{ik} \left(\sum_{k=1}^{N/2} \frac{1-\rho_i^2}{1-2\rho_i \cos\left(2k\pi/N\right)+\rho_i^2} \right)^{-1}. \tag{4}$$

Removal of the red spectrum $\hat{s}_{ik}$ from s_{ik} accentuates the anomalies and balances the signals between the tropics and Westerlies for the EOF analysis. This method, which resolves all frequencies simultaneously, is designed to analyze a single spectrum at each grid point. The autocorrelation no longer applies when band or ensemble averages are used making it difficult to estimate statistical errors.

The EOFs are constructed numerically to capture the dominate patterns within a data set independent of the underlying physical processes. For illustration, the spectral density s_{ik} can be expanded as

$$s_{ik} = \phi_{il} z_{lk}, \tag{5}$$

where ϕ_{il} denotes the EOF or spatial eigenvector for mode l and z_{lk} is the principle component for frequency k. The orthogonal eigenvectors give rise to $\phi_{il}\,\phi_{li} = \delta_{ii}$ and $z_{ik}\,z_{kl}/N = \lambda_l \delta_{ll}$, in which δ is the Kronecker delta and λ_l are the eigenvalues determined from $|C_{il} - \lambda_l \delta_{ll}| = 0$, where $C_{il} = s_{ik}\,s_{kl}/N$ is the covariance matrix. Each eigenvalue describes a fraction of the variance given by

$$\sigma_l^2 = \lambda_l \bigg/ \sum_{m=1}^{M} \lambda_m, \tag{6}$$

which indicates the contribution and ranking of the corresponding mode. The evenly spaced data points in longitude and latitude, when projected onto a sphere, distort the variance. The spectral density s_{ik} is premultiplied by $\sqrt{\cos\left(\psi\right)}$ to equally weight the covariance matrix across the latitude ψ. The same procedure is applied to the spatial-temporal data x_{ij} to determine the eigenmodes and principle components in the time domain.

4. Climate Indices

Researchers have developed a number of indices to describe climate cycles observed across the globe. These climate indices were initially defined regionally, where the phenomena are most prominent [*Walker and Bliss*, 1932, 1937]. For example, the sea level pressure anomalies between Iceland and Portugal provide the index for the North Atlantic Oscillation (NAO) [*Hurrell and Deser*, 2010]. *Thompson and Wallace* [1998] considered the regional oscillations to be subsets of larger hemispheric phenomena and defined a zonally symmetric pattern known as the Arctic Oscillation (AO) or the Northern Annular Mode from the first EOF of multiple atmospheric variables. *Deser* [2000] showed the AO and the NAO are nearly identical in the Northern Atlantic Ocean. An equivalent oscillation mode exists in the Southern Hemisphere with regional impacts [*Gillett et al*., 2006]. The phenomenon is known as the Antarctic Oscillation (AAO), which is defined by the first EOF of the geopotential height.

The NOAA Climate Prediction Center publishes the AO and AAO indices based on the procedures of *Thompson and Wallace* [1998] using the R1 data set. We define the equivalent indices using CFSR to assess the phenomena within the data set. The monthly mean 1000 and 700 mb geopotential height anomalies are created by removing the seasonal cycles for the Northern (20–90°N) and Southern (20–90°S) Hemispheres on a 2.5° × 2.5° grid. Figure 1 shows the spatial distributions of the AO and AAO for the base period 1979–2000 that closely correspond to the published loading patterns associated with the zonal structures (http://www.cpc.ncep.noaa.gov/products/). Pressure anomalies from the CFSR data set spanning 1979–2009 are projected onto the computed eigenvectors. The resulting time series is normalized by its standard deviations from the base period to provide the corresponding indices shown in the top two plots of Figure 2. Comparison between the computed and published indices shows high correlation coefficients of 0.98 and 0.91 for the AO and AAO.

In contrast to the AO and AAO, the El Niño-Southern Oscillation (ENSO) has the strongest signature in the equatorial Pacific with climate implications across the globe. Indicators of the ENSO include atmospheric pressure and temperature anomalies across the Pacific. The Southern Oscillation Index (SOI) denotes the difference of the sea level pressure anomalies between Papeete, Tahiti and Darwin, Australia normalized by its standard deviation [*Trenberth*, 1984]. The Nino 3.4 index is defined by the spatially averaged temperature anomaly in the region over (190–240°E, 5–5°N) normalized by its standard deviation. We compute the Nino

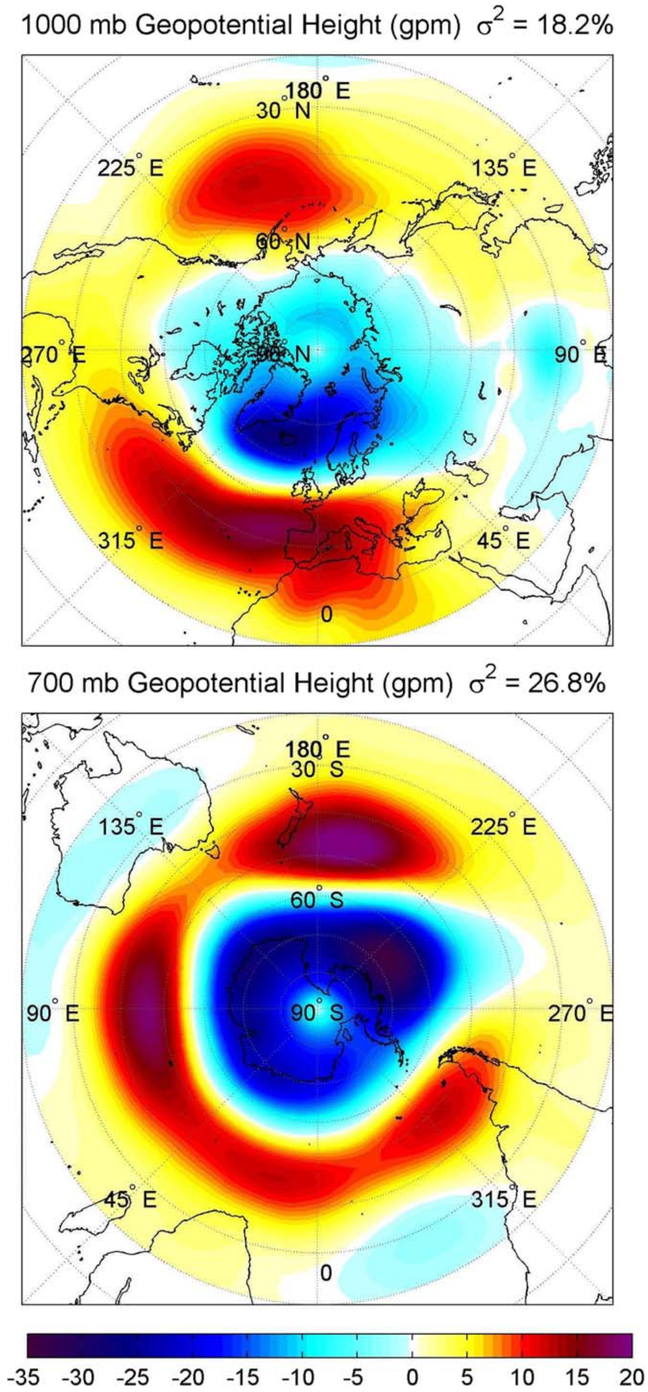
1000 mb Geopotential Height (gpm) σ^2 = 18.2%

700 mb Geopotential Height (gpm) σ^2 = 26.8%

Figure 1. (top) Mode 1 EOF from the CFSR 1000 mb geopotential height anomaly in the Northern Hemisphere defining the Arctic Oscillation. (bottom) Mode 1 EOF from the CFSR 700 mb geopotential height anomaly in the Southern Hemisphere defining the Antarctic Oscillation.

3.4 index to quantify the ENSO signals in CFSR. The computed index shown in the bottom plot of Figure 2 gives a high correlation coefficient of 0.96 with that calculated by *Smith et al*. [2008] from the Extended Reconstructed Sea Surface Temperature based on observations.

The Indian Ocean has a particularly interesting oscillation resulting from the monsoons in Southeast Asia [*Saji et al*., 1999]. One way to measure the strength and phase of the oscillation is through the sea surface temperature anomalies. The cycle, known as the Indian Ocean Dipole (IOD), is gauged by the difference of the average temperature between the western (50–70°E, 10°S–10°N) and eastern (90–110°E, 10°S–0°N) Indian Ocean [*Saji et al*., 1999]. The index is derived from the Hadley Centre Sea Ice and Surface Temperature data set [*Rayner et al*., 2003]. The IOD, which is associated with coupling of the sea surface temperature dipole and the zonal winds, has immediate effects in the monsoon region with floods observed in East Africa and drought in Indonesia. The regional oscillation has far-reaching teleconnections in Western Australia rainfall extremes and impacts on the northwestern Pacific anticyclones [*Ummenhofer et al*., 2009; *Jiang et al*., 2013].

The climate indices provide a reference to assess the variability of ocean winds and waves. The AO, AAO, and Nino 3.4 indices are calculated from CFSR twice a month to match the preprocessed wind and wave time series. The computed indices allow evaluation and elucidation of the respective phenomena within the data sets. The in situ measurements in the published SOI and the NAO and IOD indices allow validation of the complex climate dynamics in CFSR and add an element of realism to the assessment. While the selected indices describe climate oscillations with global influences, it is important to mention that other oscillations play a role in regional cycles of winds and waves. For instances, *Barston and Livezey* [1987] described the large-scale and regional climate through the top 10 EOFs of modeled pressure over the Northern Hemisphere spanning 1950–1984 and *Izaguirre et al*. [2011] and *Shimura et al*. [2013] showed certain areas are more sensitive to regional rather than large-scale oscillations.

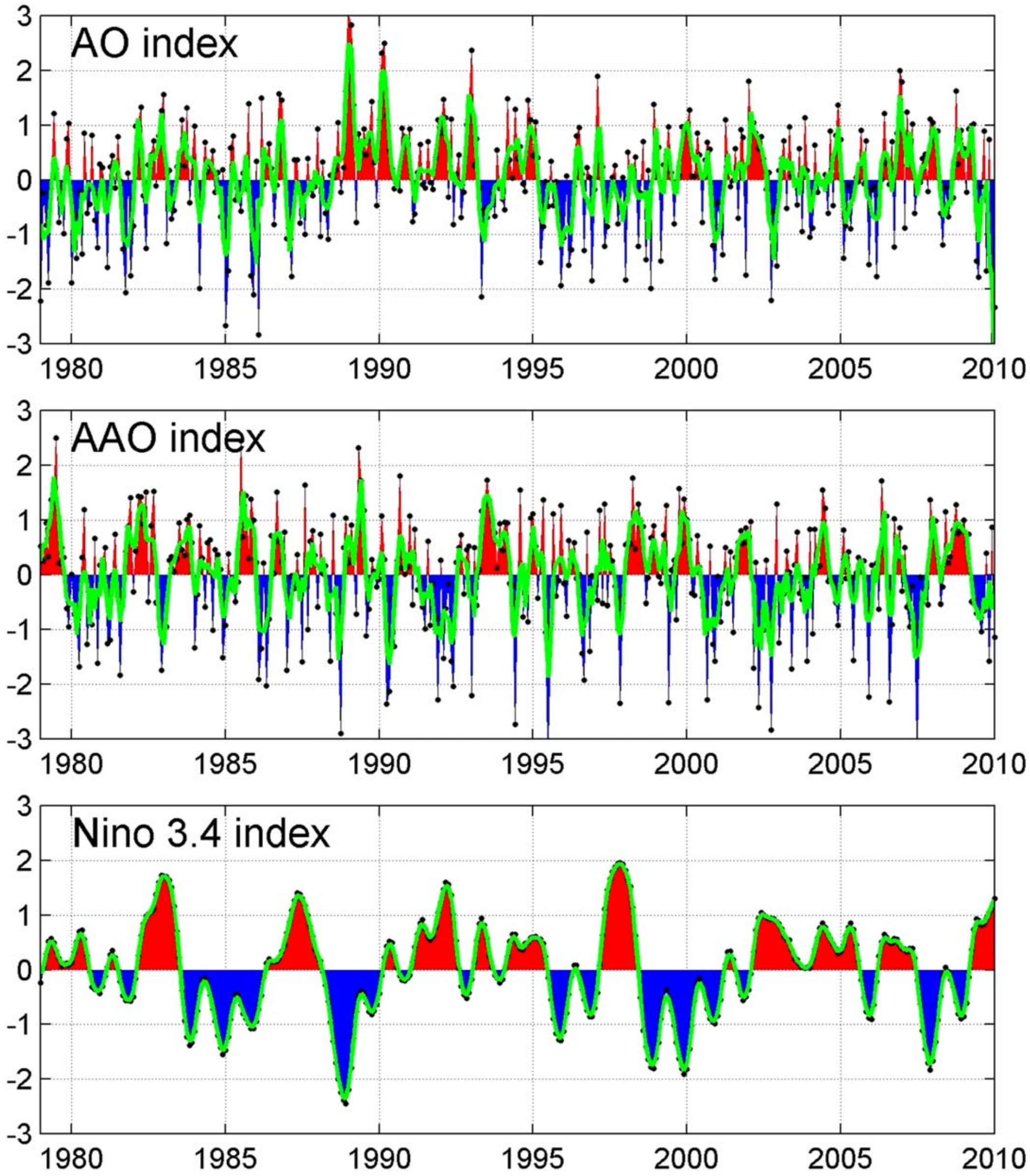

Figure 2. Monthly climate indices computed from CFSR. Green denotes a 3 month running mean, red is positive, and blue is negative.

5. Results and Discussion

Recent studies have applied climate indices to explain the inter-annual wave variability in the North Atlantic [*Bacon and Carter*, 1991; *Swail and Cox*, 2000; *Woolf et al*., 2002; *Gulev and Grigorieva*, 2006], North Pacific [*Graham and Diaz*, 2001; *Tsai et al*., 2012; *Bromirski et al*., 2013], Southern Ocean [*Hemer et al*., 2008, 2010; *Bosserelle et al*., 2011], Northern Hemisphere [*Shimura et al*., 2013], and globally [*Chen et al*., 2002; *Sterl and Caires*, 2005; *Young*, 1999; *Izaguirre et al*., 2011; *Fan et al*., 2012; *Stopa et al*., 2013a]. The EOF approach in the time domain allows comparison with findings from previous studies and provides a basis to relate the frequency domain results. To avoid masking of regional variability by dominating global signals, we separate the analysis into the three major basins: Atlantic, Indian, and Pacific and then discuss their teleconnections and global implications. The computed EOFs are correlated with four relevant climate indices in each basin, with at least one from observations independent of the CFSR data set. While the discussion focuses on climate cycles and patterns in the CFSR data sets, the supporting information provides results from a parallel analysis of ERA-I for reference and verification.

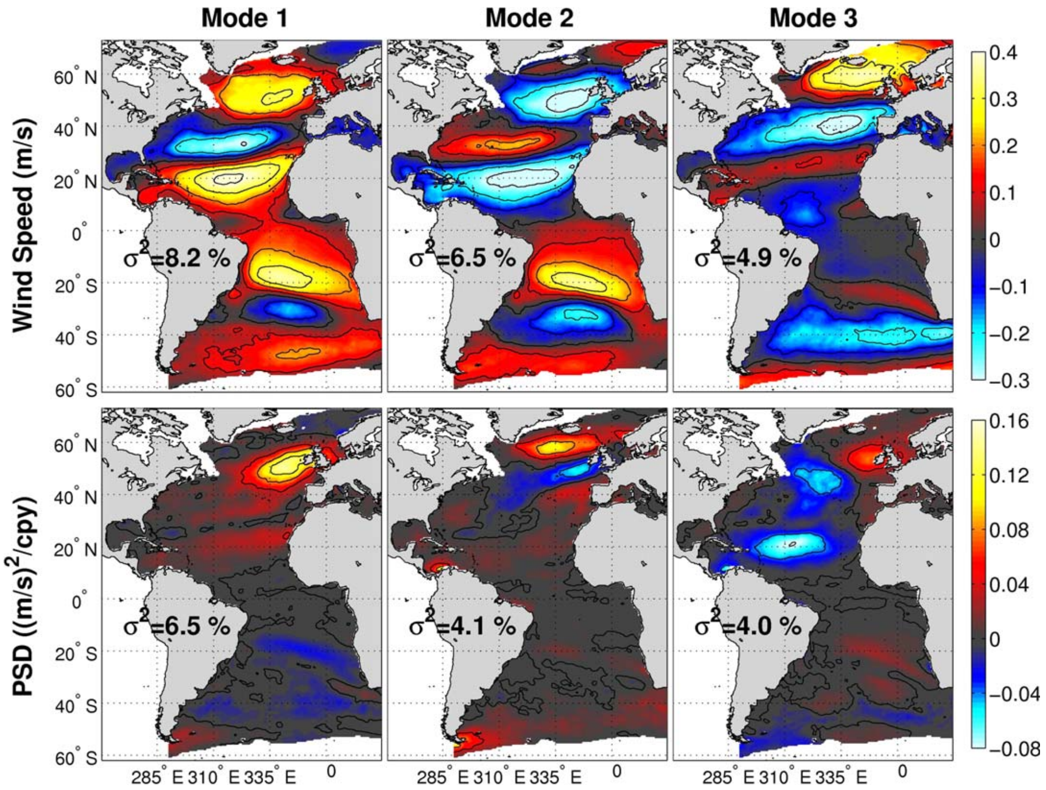

Figure 3. Wind speed EOFs from the (top) time domain analysis and (bottom) frequency domain analysis for the Atlantic Ocean.

5.1. Atlantic Ocean

The wave climate in the North Atlantic has been investigated more than any other region with numerous studies describing its variability in terms of the AO [*Bauer*, 2001; *Swail and Cox*, 2000; *Cox and Swail*, 2001; *Wang and Swail*, 2001; *Woolf et al*., 2002; *Gulev and Grigorieva*, 2006; *Izaguirre et al*., 2011; *Fan et al*., 2012]. The North Atlantic is largely seasonal with energetic waves in the boreal winter and calm conditions in the summer, while the South Atlantic has less variation throughout the year. The first three EOFs of the wind data set in Figure 3 display the dominant modes of variability in time and frequency. In the time domain, the modes depict the zonal wind regions: Westerlies in 30–60°, trade winds in 30–10°, and calm conditions near the Equator. The opposing signs in the Westerlies represent shifting of the upper level jet during the annual cycle. Qualitatively these three modes match those calculated from a yearly January-February-March averaged time series based on R1 [*Wang and Swail*, 2001]. In particular, modes 1 and 3 best represent the positive phase of the AO, while mode 2 represents the negative phase.

The bottom plots of Figure 3 show the EOFs of the power spectral density (PSD) from the frequency domain analysis. The results complement the time domain EOFs by isolating the oscillatory signals. All three modes show dominant features of the AO with distinct peaks in the Westerlies of the North Atlantic. Mode 1 has a single peak west of the British Isles associated with the average condition of the AO. The dipoles in modes 2 and 3 represent its east-west and north-south variations associated with shifting of the Westerlies. While mode 2 qualitatively represents a classic AO pattern similar to the index definition in Figure 1, mode 3 shows a more pronounced east-west split of the oscillation. The results also show signals associated with the North Atlantic trade winds. In particular, mode 3 has a distinct peak in the trade wind region east of the Caribbean Islands that might be associated with the ENSO because this region was well correlated to the phenomena by *Stopa et al*. [2013a]. In comparison to the time domain EOFs, the South Atlantic has much reduced energy with the exception of the localized peak near the Strait of Magellan south of Chile.

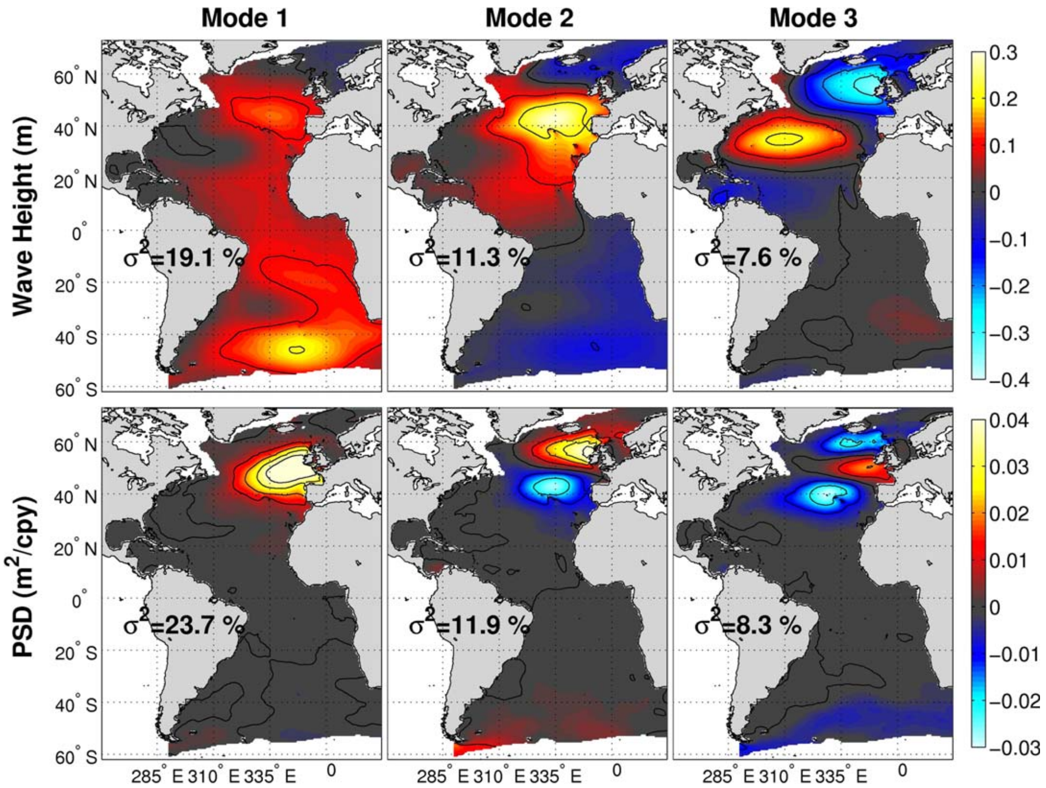

Figure 4. Significant wave height EOFs from the (top) time domain analysis and (bottom) frequency domain analysis for the Atlantic Ocean.

The propagation of swells across the ocean creates strong covariance in time and space that results in the large variances explained by the EOFs of the wave field as shown in Figure 4. The time domain EOFs have the largest amplitude in the Westerlies. Mode 1 has one common feature across the ocean with peaks in the North and South Atlantic. The pattern reflects the wave generation regions in the Westerlies and saturation of swell toward the eastern side of the ocean. The results are corroborated by the EOF analysis of the ERA-40 data set from *Sterl and Caires* [2005]. The larger fetch in the South Atlantic as pointed out by *Alves* [2006] is able to create an energetic swell field, while the North Atlantic shows a stronger relationship to the wind waves [*Semedo et al*., 2011]. Mode 2 shows opposing phases in the North and South Hemispheres. Although the annual cycle and the associated higher harmonics have been removed, the transition seasons remaining in the anomaly time series account for this north-south variation. Mode 3 best represents the structure of the AO with high energy in the North Atlantic. This mode resembles the first EOF of *Wang and Swail* [2001] from their 40 year wave data set generated by R1, *Semedo et al*. [2011] from ERA-40, and *Gulev and Grigorieva* [2006] from ship observations.

The EOF analysis in the frequency domain captures strong repeating patterns associated with the wave climate. The results shown in the bottom plots of Figure 4 are similar to the corresponding EOFs of the wind fields in Figure 3. Mode 1 shows a dominant and isolated peak west of the British Isles associated with the AO. The resemblance to the wind results implies this mode has dominant cyclic features related to the wind waves with only subtle effects from the basin-wide swells. *Sterl and Caires* [2005] suggested the wave pattern of the AO is strongly associated with the winds and *Gulev and Grigorieva* [2006] and *Semedo et al*. [2011] both confirm this hypothesis from independent data sets. The frequency domain analysis is able to extract more detailed features of the wave field. The dipole in mode 2 describes the north-south shifting of the dominant signal in mode 1, while mode 3 accounts its expansion and contraction in the north-south direction. Similar to the frequency domain EOFs of the winds, the waves in North Atlantic show much larger variability that masks the climate signals in the south. The only discernible feature is the weak zonal structure near Antarctica in mode 3.

Table 1. Correlation Coefficients for Principal Components and Climate Indices in the Atlantic Ocean[a]

	Time Domain			Frequency Domain		
Eigenmode	1	2	3	1	2	3
			Winds			
σ^2 (%)	8.2	6.5	4.9	6.5	4.1	4.0
NAO	+0.27*	−0.18*	+0.25*	+0.20*	+0.34*	+0.16*
AO	+0.15*	−0.14*	+0.33*	+0.10	+0.40*	+0.32*
AAO	−0.02	−0.02	+0.16*	+0.02	+0.14	+0.17*
Nino 3.4	−0.19*	−0.06	−0.07	−0.04	+0.27*	+0.37*
			Waves			
σ^2 (%)	19.1	11.3	7.6	23.7	11.9	8.3
NAO	+0.10	−0.09	−0.38*	+0.22*	+0.31*	+0.36*
AO	+0.05	−0.13*	−0.36*	+0.05	+0.30*	+0.32*
AAO	−0.08	+0.01	−0.08	−0.01	+0.08	+0.17*
Nino 3.4	−0.07	−0.00	+0.10	−0.09	+0.22*	+0.22*

[a] Asterisks denote the statistical significance at the 95% level.

The principal components are correlated with the semimonthly time series and computed spectra from the AO, AAO, and Nino 3.4 indices based on the CFSR data set. In addition, correlation with the NAO index from in situ pressure data provides an external source of information for reference. Table 1 summarizes the correlation coefficients for the first three modes to provide quantitative interpretations of the climate

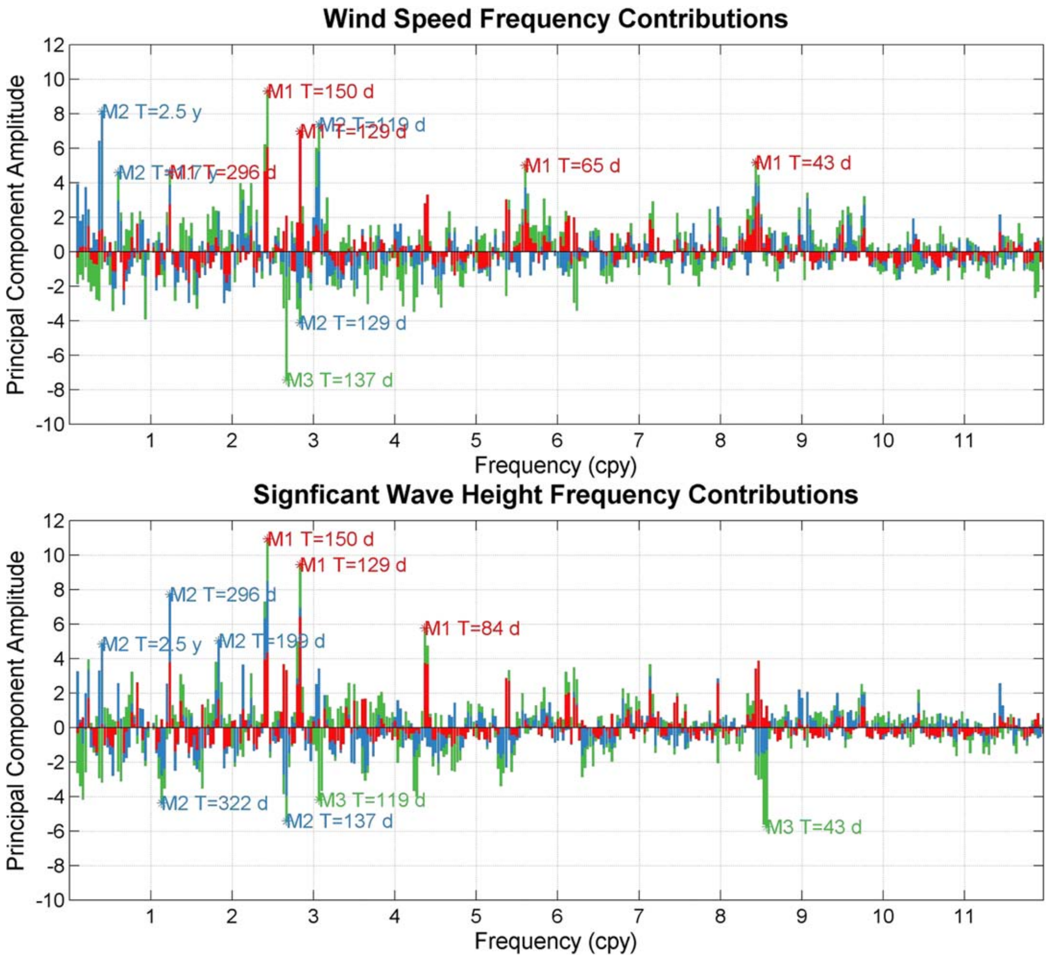

Figure 5. Principal components for the (top) wind speed and (bottom) significant wave height in the Atlantic Ocean. Red denotes mode 1, blue mode 2, and green mode 3 with top 10 components annotated.

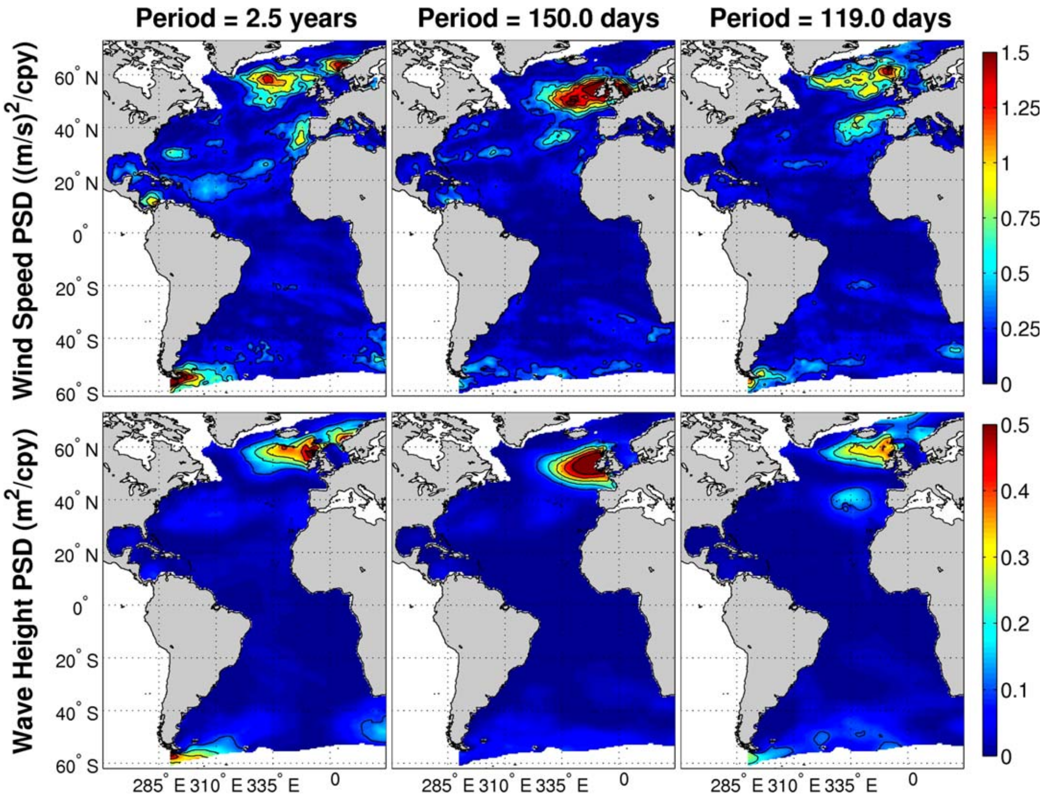

Figure 6. Power spectral density from representative periods for the (top) wind speed and (bottom) significant wave height in the Atlantic Ocean.

associations for the EOFs. Since the sign of the EOFs is arbitrarily assigned, only the magnitude of the correlation coefficients is meaningful. Statistically significant values are denoted by an asterisk when the p value $\leq$0.05. For the wind data set, the zonal structure of the EOFs from the time domain analysis is related to the AO and NAO. These indices are very similar in the North Atlantic and the results support the findings of *Deser* [2000]. The correlation in the frequency domain gives a measure of the matching spectral components with the climate indices. All three principal components have a relationship with the AO, but mode 2 best captures the oscillation. The ENSO generally has a weak influence in the Atlantic but shows statistical significant correlation in modes 2 and 3.

The correlation coefficients of the waves follow similar patterns as the winds; however, the values of the explained variance are typically larger. In the time domain, modes 1 and 2 have very weak correlation with the tested climate signals as shown by the low values in Table 1. The EOFs in Figure 4 depict average swell conditions in mode 1 and seasonal variations in mode 2 that are not described by the climate indices. Mode 3 has the highest correlation with the NAO giving confidence that the dipole structure of the EOF does represent the climate cycle. The correlation coefficients in the frequency domain are larger. All three modes correlate well with the NAO and mode 3 has statistical significant relationships with the four tested indices. The low correlation of the AO with mode 1 might be due to the fact that the indices are defined by pressure anomalies, which have different active areas compared to the waves. In addition, the analysis is computed for the entire data set including the boreal summer, when *Bauer* [2001] shows the lack of a relationship with the AO. The correlation coefficients for the AAO and ENSO would be larger if separate regional analyses were performed (not shown).

We plot the principal components of the winds and waves in Figure 5 to demonstrate the dominant frequencies in the EOFs. The positive and negative values are due to subtraction of the background energy from the deseasoned spectrum. The principal components from the winds and waves have similar frequency content corroborating the similar spatial structure of the EOFs. The top 10 components from the

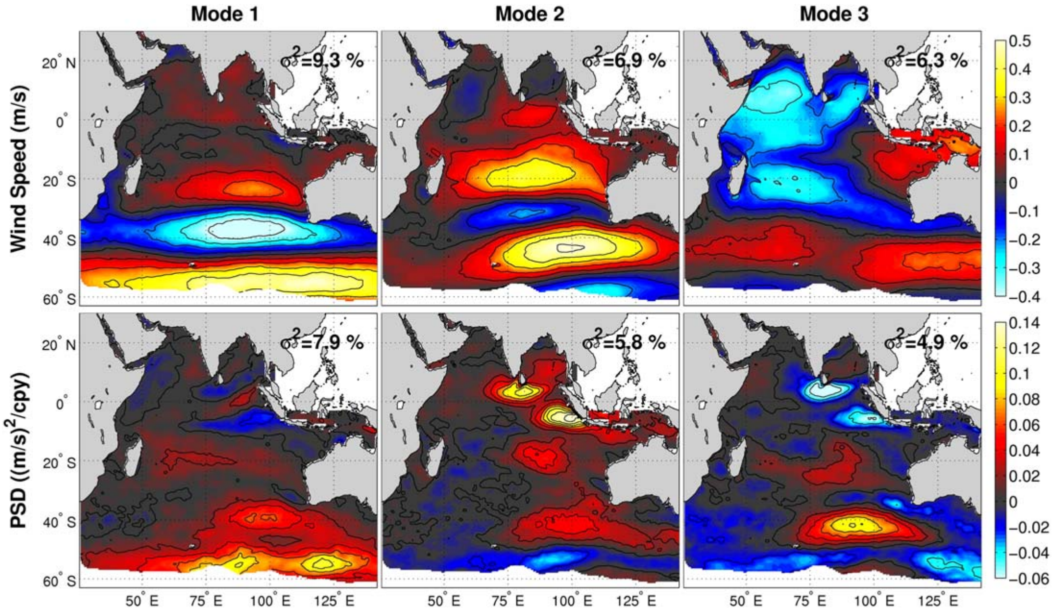

Figure 7. Wind speed EOFs from the (top) time domain analysis and (bottom) frequency domain analysis for the Indian Ocean.

three modes are annotated with their periods. The energy is spread throughout the frequencies with the largest peaks in the intra-annual band of 100–300 days period. There is some energy in the inter-annual range, but it is on the same scale as the 40–100 day oscillations. The broad-band signals of the EOFs support the dynamic nature of the North Atlantic Ocean [*Sterl et al*., 1998]. However, the climate cycles are often described by their inter-annual variability in the literature [e.g., *Wang and Swail*, 2001; *Sterl and Caires*, 2005; *Fan et al*., 2012; *Stopa et al*., 2013a; *Bromirski et al*., 2013]. The results show that the intra-annual and inter-annual oscillations have similar magnitude and comparable roles in basin-scale climate cycles.

The EOF and correlation analyses have identified frequency components of relevance to the climate cycles. Figure 6 shows the spectral density distributions of the winds and waves at selected periods. The 2.5 year component has prominent peaks near 55°N and S. The peaks in the North Atlantic and the North Sea appear to be connected and most likely related to the AO [*Bauer*, 2001; *Wang and Swail*, 2001]. Higher resolution regional analyses can better quantify the relationship. The spectral density of the winds also shows a feature offshore of Portugal that extends across the trade wind region to the Caribbean Sea. The feature is filtered in the wave field because the trade winds are not a dominant wave energy source. The 150 day period shows a dominant feature centered west of the British Isles as seen in mode 1 of the EOF. *Stopa et al*. [2013a] shows strong correlation of this region with the AO suggesting that the 150 day oscillation is an important component of the climate cycle. The 119 day component has peaks at 40°N and 60°N that align with the two phases of the AO as shown in the EOF of the geopotential height in Figure 1. All examples show the strongest signals in the North Atlantic with relatively subtle, but detailed features around Antarctica. The periodicity and patterns presented here provide new information on the AO, which is known to dominate the North Atlantic.

5.2. Indian Ocean

The North Indian Ocean has a unique weather pattern that reverses its wind and wave direction over an annual cycle associated with the monsoon. The large-scale pressure system migrates north-south driving the atmosphere circulation in Southeast Asia. The wind flow is predominately from the Northeast during the winter months of October to March and from the Southwest during the summer months of June to August. The pressure migration provides the initial forcing to create large sea-surface temperature anomalies that drive the regional dynamics and change the wind flow near the Equator [*Saji et al*., 1999]. The year-round southeast trade winds in the region 10–30°S generate waves that propagate into the North Indian Ocean [*Stopa et al*., 2013a]. The swells generated by the Westerlies in 30–60°S saturate the entire basin

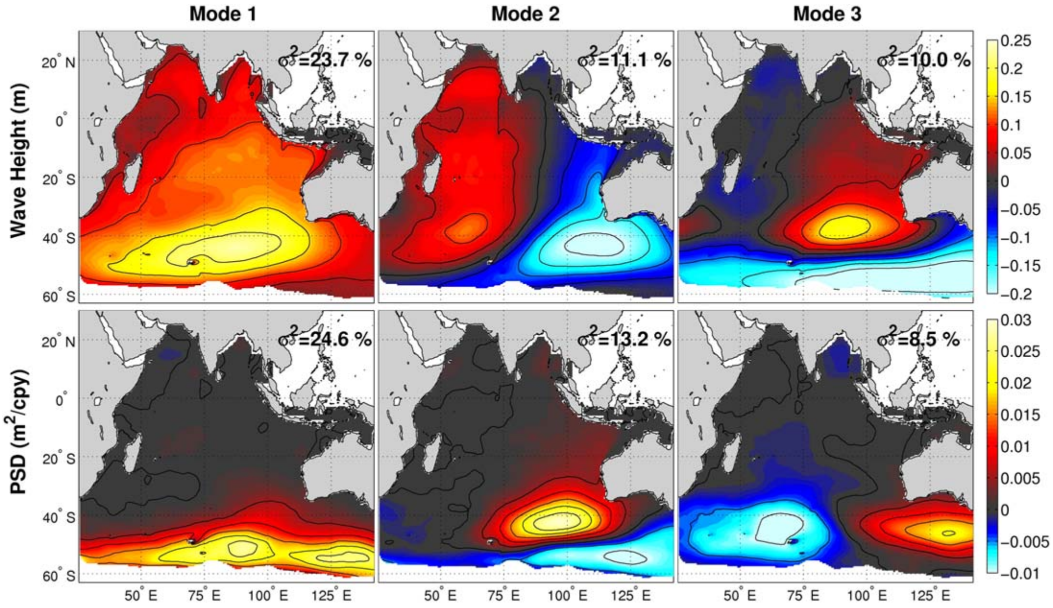

Figure 8. Significant wave height EOFs from the (top) time domain analysis and (bottom) frequency domain analysis for the Indian Ocean.

throughout the year. In particular, there is a focus of energy to the Southwest of Australia making it one of the most active wave regions on the globe [*Hemer et al*., 2010; *Bosserelle et al*., 2011].

We first analyze the wind speed to provide a reference for assessment of the wave climate. Figure 7 displays the dominant modes of variability in time and frequency. Modes 1 and 2 from the time domain analysis represent the zonal pattern of the winds. The structure in mode 1 best resembles the spatial signature of the AAO with the trimodal features demonstrated in the CFSR data set by *Stopa et al*. [2013a]. Mode 2 has similar zonal features across the ocean, but with a slightly shifted three-band pattern in comparison to the classic AAO signature. Mode 3 exhibits a prominent feature across the Westerlies and a longitudinal split near 90°E. In the Indian Ocean, the EOF has a dominant feature encompassing the ocean east of Madagascar extending across the Equator to the Arabian Sea and the Bay of Bengal. This western portion of the ocean has an opposite phase to the eastern half centered between Indonesia and Australia. The opposing sign in the east-west direction near the Equator is related to the Monsoon.

The bottom plots of Figure 7 show more distinct features of the EOFs from the frequency domain analysis. The three modes have similar spatial patterns albeit with different amplitudes and phases. Each mode has a zonal structure across the Westerlies at 55°S and a distinct feature Southwest of Australia at 40°S. These two features have the same phase in mode 1, but opposing phases in modes 2 and 3. The prominent peaks west of Indonesia and south of India, which correspond to the IOD indicator regions defined by *Saji et al*. [1999], have opposite signs between modes 2 and 3. There are weaker, but systematic signals in the trade wind region between 15°S and 25°S across the Indian Ocean. A mid-ocean feature is well defined in mode 2 near (85°E, 20°S) with the same sign as in the IOD regions to the north, but in modes 1 and 3, this feature is more spread out and has opposing signs with respect to the IOD. The coherent signals across the Westerlies, trade wind, and IOD regions illustrate the complexity of the basin-wide and regional dynamics.

The dominant modes of variability in the wave field exhibit a different pattern from the winds. In Figure 8, the time domain EOFs show predominantly north-south variation of the signals, while the frequency domain analysis isolates their sources in the south. Mode 1 in the time domain represents the year-round swells across the entire basin. In the frequency domain, mode 1 captures the source from the persistent extratropical cyclones in the Westerlies. Mode 2 in the time domain and mode 3 in the frequency domain have two opposing regions in the east-west direction. The meridional dipole represents seasonal shifts of the storms and the resulting modulation of the swells between the eastern and western halves of the ocean. Mode 3 in the time domain shows two opposing features in the Southern Indian Ocean with a clear zonal structure akin to the AAO. The extratropical cyclones track closer to Antarctica during the positive

Table 2. Correlation Coefficients for Principal Components and Climate Indices in the Indian Ocean[a]

	Time Domain			Frequency Domain		
Eigenmode	1	2	3	1	2	3
			Winds			
σ^2 (%)	9.3	6.9	6.3	7.9	5.8	4.9
SOI	−0.06	+0.10	−0.18*	+0.28*	+0.32*	+0.43*
IOD	+0.11*	−0.06	+0.21*	+0.24*	+0.71*	+0.57*
AAO	+0.42*	−0.12*	−0.11*	+0.30*	+0.19*	+0.29*
Nino 3.4	+0.02	−0.11*	+0.15*	+0.28*	+0.35*	+0.47*
			Waves			
σ^2 (%)	23.7	11.1	10.0	24.6	13.2	8.5
SOI	+0.08	−0.08	−0.15*	+0.30*	+0.39*	+0.23*
IOD	−0.05	+0.04	+0.20*	+0.22*	+0.11	+0.06
AAO	+0.02	−0.04	+0.37*	+0.16*	+0.28*	+0.09
Nino 3.4	−0.03	+0.03	+0.13*	+0.23*	+0.30*	+0.14

[a] Asterisks denote the statistical significance at the 95% level.

phase of the AAO and generate larger waves due to an unimpeded fetch extending from the South Atlantic to the South Pacific as represented by the continuous negative region in the EOF. The developed swells can propagate across the western half of the basin reaching the Arabian Sea. When the AAO index is negative, the extratropical cyclones are centered near 40°S. The cut off of the fetch by Africa results in shifting of the heightened wave activities to the eastern half of the basin with a large positive region in the EOF Southwest of Australia. Mode 2 in the frequency domain better represents the signal sources with its strong zonal structure in the eastern half of the basin.

Table 2 provides the correlation coefficients between the climate indices and principal components to gauge the climate association of the EOFs. The AAO and Nino 3.4 indices are computed from CFSR, while the SOI and IOD are defined from independent data sets. Mode 1 of the wind field in the time domain has the strongest relationship with the AAO, while mode 2 has relatively weak correlation with the AAO and ENSO. Mode 3 appears to comprise all four climate indices with the best relationship with the IOD. Separate regional analysis based on the spatial structures in Figure 7 will better illuminate each mode's climate association. In the frequency domain, the correlation coefficients of the wind fields from all three modes are related to the ENSO, AAO, and the IOD at the 95% confidence level. In particular, mode 2 matches the source regions of the IOD resulting in the strongest relationship compared to the other indices. The significant correlation reveals the good match of the frequency contents of the principal components and climate indices. However, the EOFs are mixing the phenomena and perhaps the 31 years of data is not long enough to fully resolve the inter-annual cycles. An interpretation for the significant correlation is that the frequency components of the climate cycles are similar and possibly interact nonlinearly making it difficult even in the frequency domain to pinpoint the distinct cycles.

The correlation coefficients of the waves have some similarities with the winds, even though the explained variances are significantly larger due to the presence of swell. In the time domain, modes 1 and 2 do not relate to the climate indices. Their low correlation should not be construed as the lack of impact to the ocean environment. Mode 3 best matches the AAO and has small influences from the IOD and ENSO. In the frequency domain, mode 1 captures all the tested climate cycles with the strongest correlation to the ENSO. Although mode 2 in Figure 8 qualitatively resembles the AAO, its principal components describe the AAO and ENSO equally well. The strong linkage to the SOI suggests influences of the swell field from the ENSO via the wave generation region in the Southern Indian Ocean. Previous studies have demonstrated strong correlation between these two climate cycles in the Indian Ocean [*Turner*, 2004; *Carvalho et al*., 2005; *Pezza et al*., 2012]. Mode 3 has significant correlation with the ENSO through the SOI, which was calculated from in situ pressure data. The weaker correlation with the Nino 3.4 index could be due to its definition from variables and locations less representative of the wave conditions in the Indian Ocean.

The principal components in the frequency domain illuminate the compositions of the EOFs by period. Figure 9 shows the majority of the wind energy in the inter-annual band of 1.6–5 years. The waves have

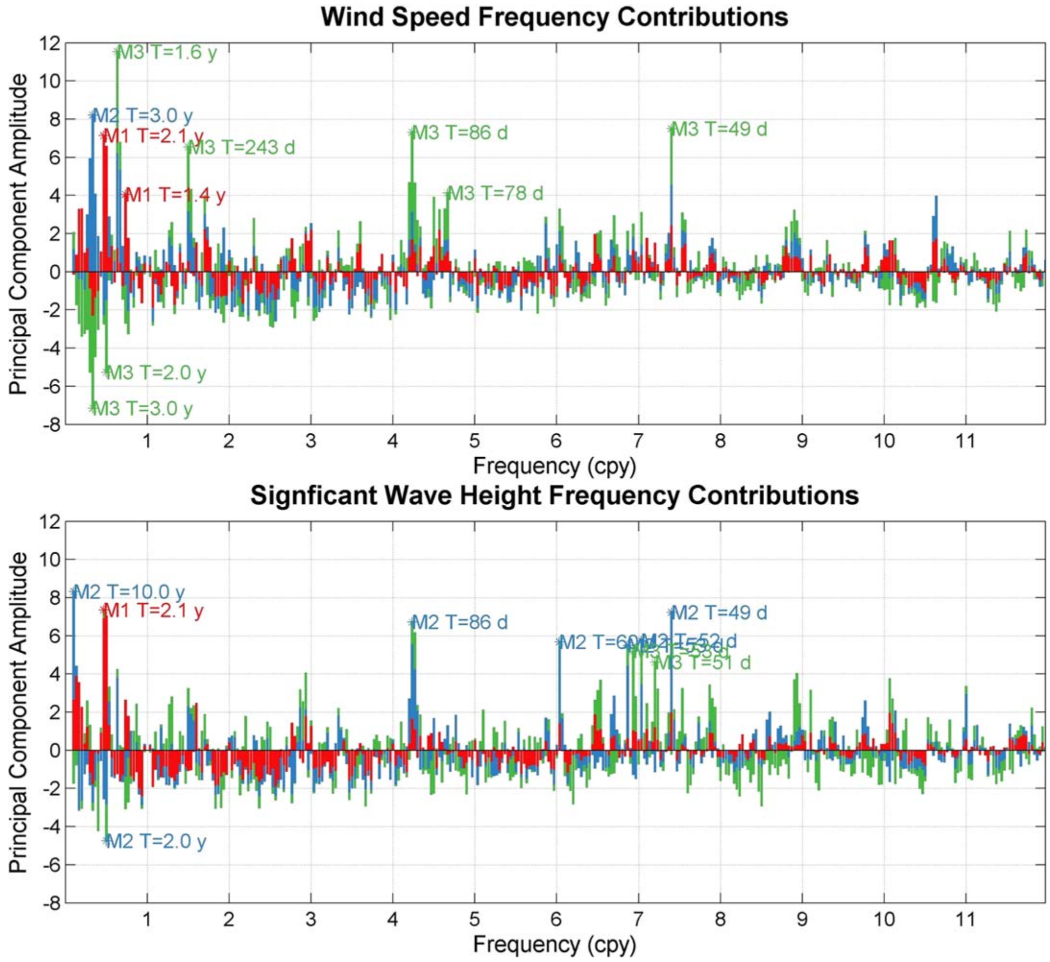

Figure 9. Principal components for the (top) wind speed and (bottom) significant wave height in the Indian Ocean. Red denotes mode 1, blue mode 2, and green mode 3 with top 10 components annotated.

less energy in this band, but exhibit a distinct peak with a period of 2.1 years. The ENSO has periods of 2–7 years and is the largest global climate signal on the inter-annual scale [*Neelin et al*., 1998]. This explains why the various modes always have weak to moderate correlation with the ENSO. In addition, both the winds and waves have dominant components in the 50–60 and 80–90 day ranges coincident with the Madden-Julian oscillation (MJO) [*Madden and Julian*, 1972]. Figure 10 shows three representative oscillations from the Fourier transform of the winds and waves. The wave fields are analogous to a smoothed version of the winds with prominent peaks in the Westerlies. Both the winds and waves at 2.1 years period show a dominant zonal structure along 55°S and a weaker band along 40°S representative of the AAO structure. The wind field at the 1.6 years period has distinct peaks in the equatorial, trade wind, and Westerlies regions along 90°E. This period has contributions in all three EOFs with correlation to the IOD among other cycles. Only the peak in the Westerlies is apparent in the wave field as this is a generation region. The 49 and 86 day (not shown here) components both have a prominent peak at the same location in the Westerlies as the 1.6 year component. Both the 49 and 86 day components are within the MJO frequency band suggesting linkage between the wind and wave signatures to this climate cycle.

5.3. Pacific Ocean

The Pacific Ocean has the largest expanse of unimpeded water and represents an important driving force of the global wave climate. The Southern Pacific is connected to the Atlantic through the Indian Ocean allowing continuation of storm systems across the Westerlies and producing the most consistent and energetic waves

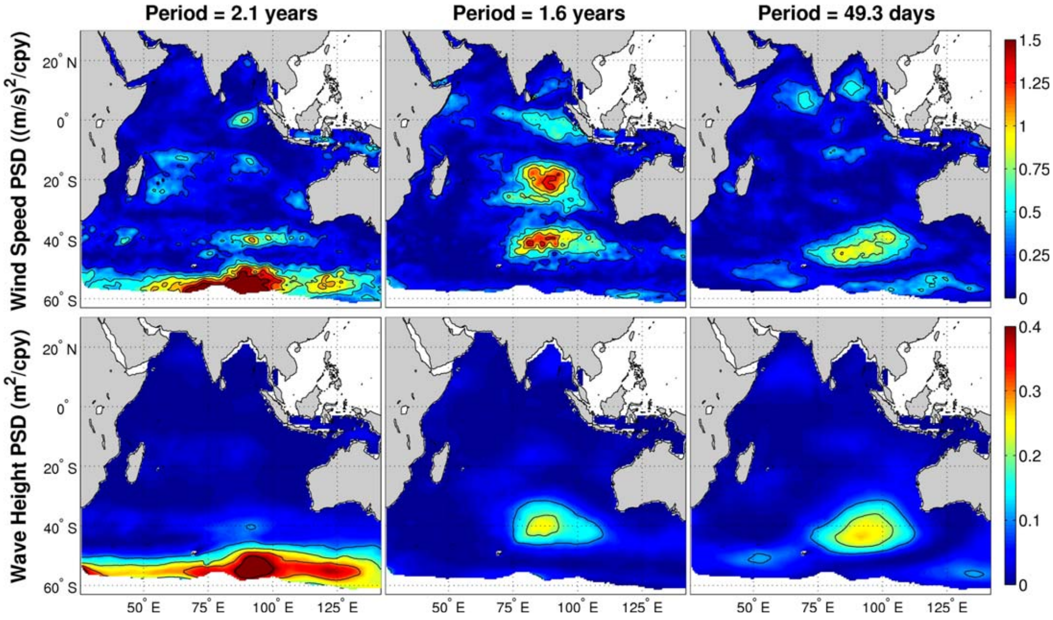

Figure 10. Power spectral density from representative periods for the (top) wind speed and (bottom) significant wave height in the Indian Ocean.

observed globally [*Hemer et al*., 2010, *Arinaga and Cheung*, 2012]. The tropics and subtropics have relatively mild Easterly trade winds, but can still generate appreciable wave activities especially in the Central North Pacific [*Stopa et al*., 2013b; *Bromirski et al*., 2013]. The North Pacific is largely seasonal with energetic waves in the boreal winter and relatively calm conditions in the summer. The wave climate in the North Pacific has been studied extensively through multiple data sets derived from R1, ERA-40, and ship observations [*Graham and Diaz*, 2001; *Wang and Swail*, 2001; *Semedo et al*., 2011; *Gulev and Grigorieva*, 2006].

We first analyze the winds to provide a basis for assessment of the wave pattern. The top plots of Figure 11 show distinct zonal structures in the first three EOFs from the time domain analysis. The respective strong

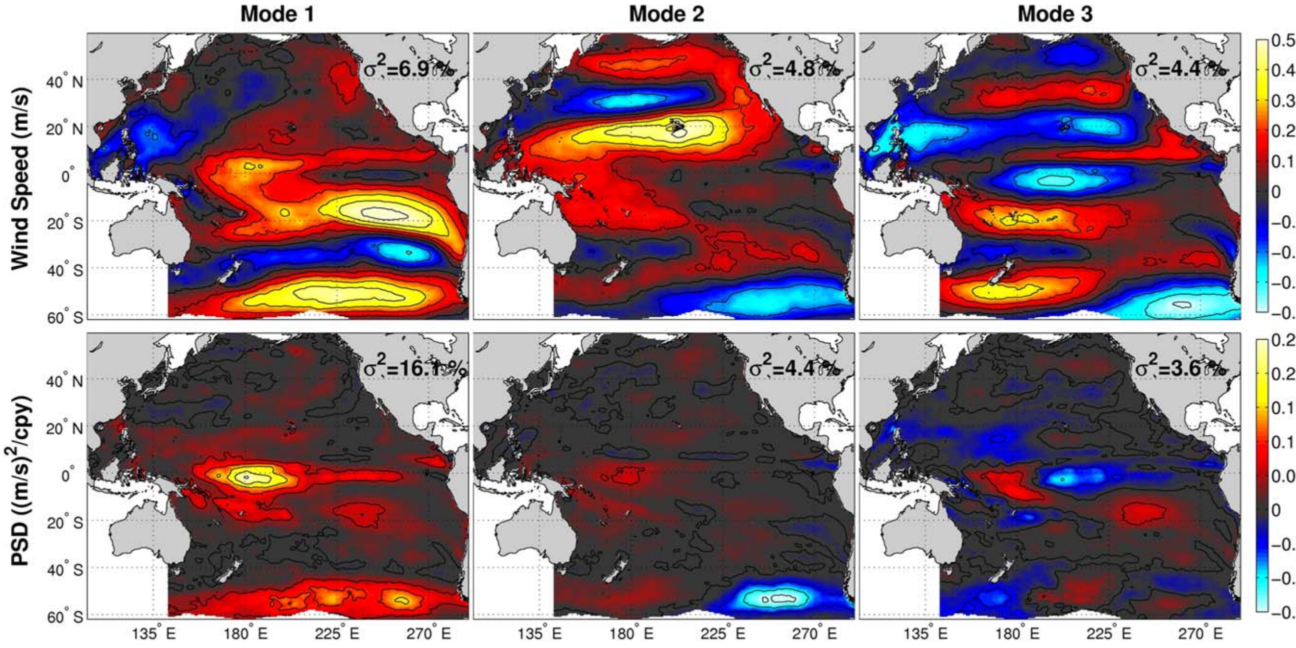

Figure 11. Wind speed EOFs from the (top) time domain analysis and (bottom) frequency domain analysis for the Pacific Ocean.

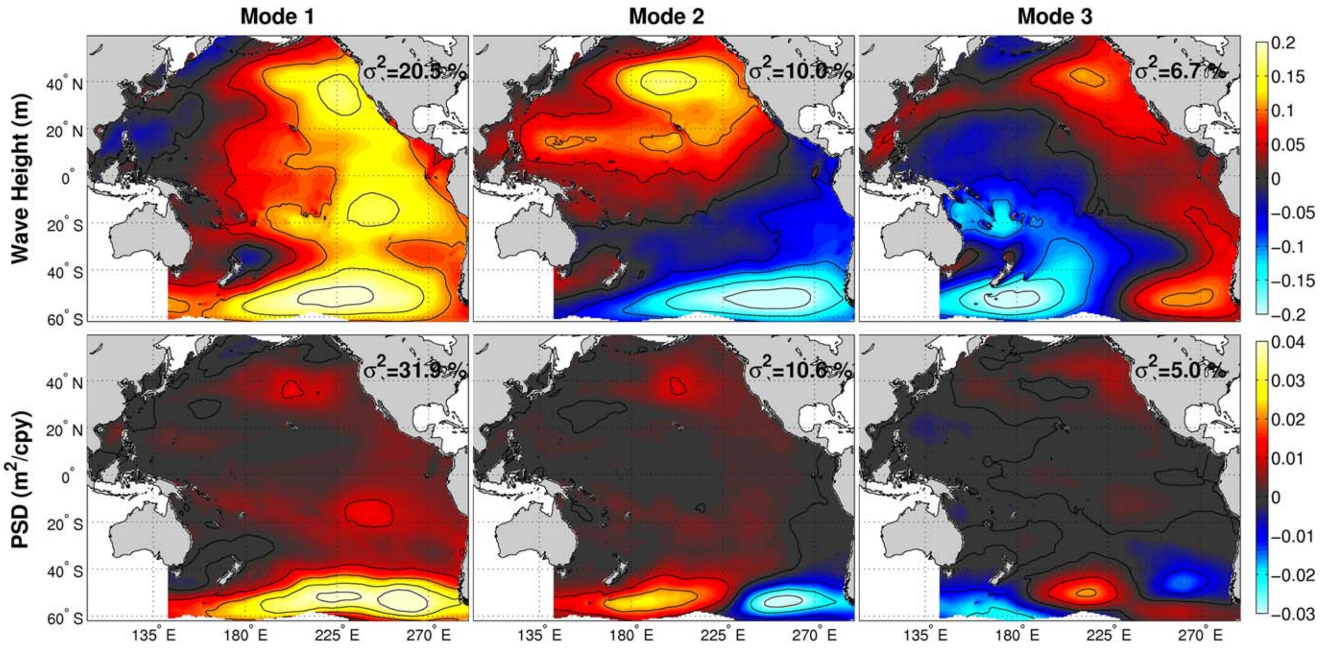

Figure 12. Significant wave height EOFs from the (top) time domain analysis and (bottom) frequency domain analysis for the Pacific Ocean.

features in the Southern and Northern Hemispheres in modes 1 and 2 are residuals of seasonal effects. The South Pacific trade wind region has an arc shape extending across the ocean from Chile associated with the subtropical jet. The North Pacific in modes 2 and 3 has a trimodal zonal structure typical to the AO, but the relationship is not as well defined as in the North Atlantic [*Deser*, 2000]. The EOF in mode 2 is reminiscent of the Pacific Decadal Oscillation (PDO) identified by *Mantua et al*. [1997]. Mode 3 has opposing signs in the eastern and western halves of the Southern Pacific. The peak near the Equator at 210°E coincides with the region of the largest inter-annual variability [*Stopa et al*., 2013a]. The region also defines the Nino 3.4 index alluding to the association with the ENSO. In addition, mode 3 captures other small features across the basin including the elongated strip at 8°N associated with the upper limit of the intertropical convergence zone. The strong feature in the South China and Philippine Seas is representative of the monsoon winds.

The frequency domain results in the bottom plots of Figure 11 better resolve the spatial pattern of the climate cycles. Mode 1, which has the largest variance among the three oceans, comprises a dominant patch along the Equator and a series of peaks extending across the Southern Pacific. The peak near the Equator at 190°E closely corresponds to the Nino 3.4 region as in mode 3 of the time domain results. The zonal feature across the Southern Ocean relates to the ENSO with signatures in the ocean currents, upper level jets, and sea ice [*Turner*, 2004; *Yuan*, 2004]. Mode 2 shows energy in similar regions, but with reduced magnitude along the Equator. The Southern Pacific has opposing features acting as an east-west dipole. In mode 3, there are two prominent peaks close to the Equator at 170°E and 200°E with opposing signs and a third peak slightly to the south near 245°E. The key features in modes 2 and 3 with opposing signs denote migration of the primary energy in mode 1 across the Southern Pacific and from South America toward and along the Equator.

The time and frequency domain analyses of the wave data set produce the EOFs shown in Figure 12. Mode 1 in the time domain resembles a mix of the swell fields from the seasonal EOFs of *Semedo et al*. [2011]. The strong features in the North and South Pacific correspond to the seasonal extremes and the peak at the center denotes the converging swells from the two hemispheres. Mode 2 represents the seasonality with opposing signs in the North and South Pacific that is still present in the anomaly time series. The Northeast-Southwest nodal line of the EOF represents the swell front found in seasonal averages of altimetry data by *Young* [1999]. The feature in the North Pacific qualitatively matches the EOFs of the wave fields derived from R1 [*Wang and Swail*, 2001; *Bromirski et al*., 2013], ERA-40 [*Semedo et al*., 2011], and ship observations

Table 3. Correlation Coefficients for Principal Components and Climate Indices in the Pacific Ocean[a]

	Time Domain			Frequency Domain		
Eigenmode	1	2	3	1	2	3
			Winds			
σ^2 (%)	6.9	4.8	4.4	16.1	4.4	3.6
SOI	+0.24*	−0.13*	−0.21*	+0.79*	+0.60*	+0.70*
AO	−0.04	+0.08	−0.15*	+0.44*	+0.32*	+0.38*
AAO	+0.21*	−0.10*	−0.07	+0.33*	+0.26*	+0.38*
Nino 3.4	−0.22*	+0.16*	+0.26*	+0.71*	+0.55*	+0.62*
			Waves			
σ^2 (%)	20.5	10.0	6.7	31.9	10.6	5.0
SOI	−0.12*	−0.20*	+0.19*	+0.59*	+0.44*	+0.43*
AO	−0.00	−0.02	−0.08	+0.40*	+0.20*	+0.24*
AAO	+0.22*	−0.20*	−0.06	+0.45*	+0.37*	+0.33*
Nino 3.4	+0.10*	+0.25*	−0.12*	+0.52*	+0.44*	+0.30*

[a] Asterisks denote the statistical significance at the 95% level.

[*Gulev and Grigorieva*, 2006]. Mode 3 shows opposing features in the east-west halves of the basin analogous to mode 2 of the wave field in the Indian Ocean. The meridional dipole represents seasonal shift of the swells between the east and west. All three modes show strong seasonal effects as elucidated in previous studies, but lack the detailed climate features of interest here.

The frequency domain EOFs in the bottom plots of Figure 12 reveal the oscillatory features of the wave field that are dominant in the Southern Hemisphere Westerlies. The three EOFs match those of the wind field in the Southern Pacific, but lack any feature near the Equator. The wave field in the equatorial region consists of swells from the North and South Hemispheres and subtle variations of the local winds do not influence the wave field above the background swell conditions. The prominent mode-1 feature is in the wave-generation region of the Southern Hemisphere extending across the longitude at 40–60°S. There are less energetic peaks in the Westerlies of the Northern Hemisphere and in trade wind region of the Southern Hemisphere. Modes 2 and 3 retain the weaker features in the North Pacific and show orthogonal variations of mode 1 that are characterized by strong opposing signals in the Southern Hemisphere Westerlies. All modes have strong signals in the major wave generating regions of the Westerlies, implying their influence on the swells in the far field.

The principal components of the wind and wave EOFs are correlated with the climate indices to quantify their relationships. The correlation coefficients in Table 3 are based on the AAO, AO, and Nino 3.4 indices derived from CFSR and the SOI from independent data sets. In the time domain, modes 1 and 2 of the wind field have weak correlation with the AAO and mode 3 has weak correlation with the AO. The opposing zonal features of modes 1 and 2 in the South Pacific and mode 3 in the North Pacific in Figure 11 corroborate these relationships. All three modes also have a weak relationship with the ENSO due to masking of the signals by seasonal effects. In the frequency domain, all the climate cycles are statistically significant to the principal components and the correlation coefficients are noticeably larger proving the efficacy of the analysis in isolating oscillatory features. The correlation coefficients of the wind field with the ENSO are consistently the largest among the oceans considered. The waves generally follow the same pattern, but show reduced correlation with the ENSO due the definition of the indices outside the generation regions.

Figure 13 shows the principal components of the first three EOFs from the frequency domain analysis. Both the winds and waves have majority of the energy in the 1.5–7 year band associated with the ENSO [*Neelin et al*., 1998; *Turner*, 2004]. There are less contributions of the EOFs in the intra-annual range comparing to the Indian Ocean. The waves have more anomalous peaks than the winds with isolated energy at 127, 119, and 70 days period. Figure 14 shows the spatial structures of the spectral energy density that significantly contribute to the EOFs. The 5 year component matches mode 1 of the wind and wave fields. The maximum variance and the strong correlation of this mode to the ENSO suggest the 5 year oscillation contains its signatures of the winds in the equatorial region and the waves in the Westerlies. At the 2.7 year period, isolated features appear in the same regions near the Equator and in the Southern Hemisphere Westerlies. In comparison to the 5 year component, the features near the Equator are much weaker, and the effect in the

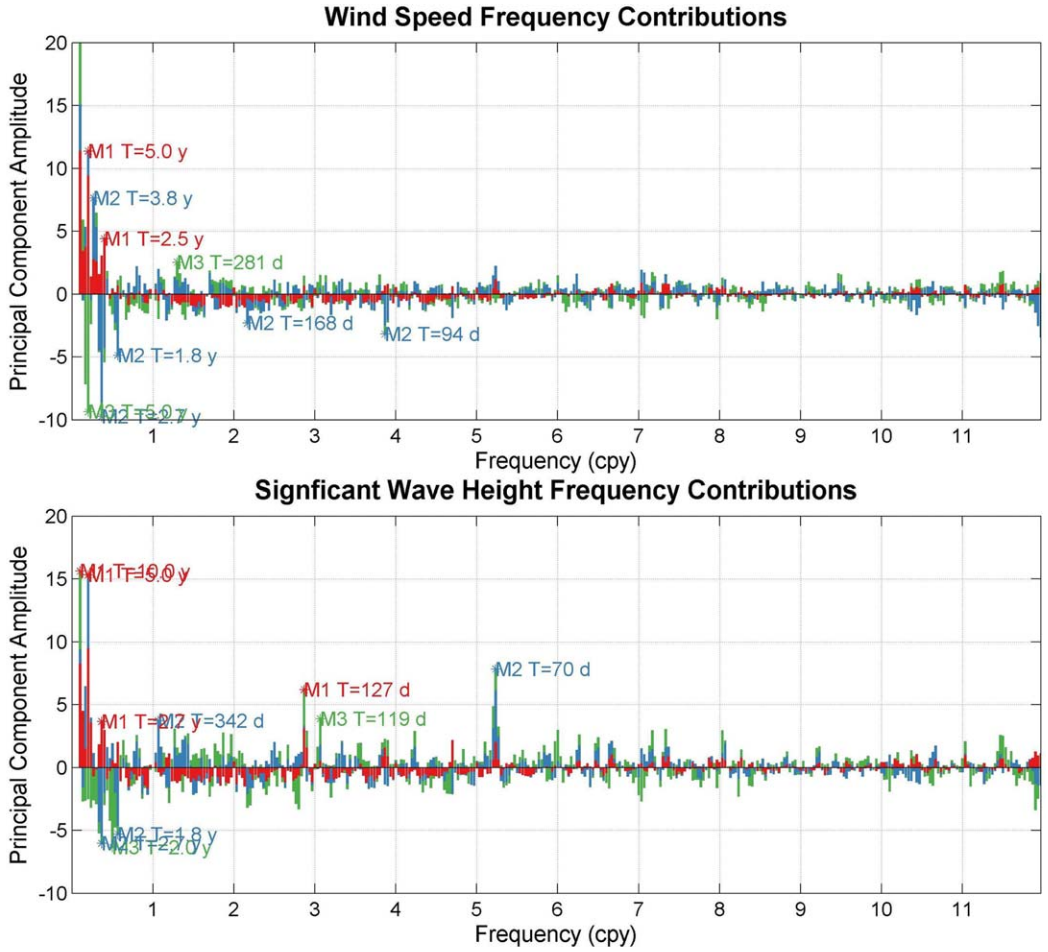

Figure 13. Principal components for the (top) wind speed and (bottom) significant wave height in the Pacific Ocean. Red denotes mode 1, blue mode 2, and green mode 3 with top 10 components annotated.

Southern Pacific is limited to the eastern half. The 70 day cycle is much weaker than the 2.7 year cycle, but each constitutes one phase of the dipole in mode 2 showing their connection to the ENSO. Due to swell propagation, the impact of the ENSO in the Westerlies has basin-wide implications. A more appropriate SOI for the waves should be defined in the Westerlies.

5.4. Teleconnections Across Basins

Climate signals have teleconnections and some of the oscillations are global phenomena. While previous studies used annual seasonal averages to analyze dominant modes of the global climate [e.g., *Wang and Swail*, 2001; *Sterl and Caires*, 2005; *Gulev and Grigorieva*, 2006; *Semedo et al*., 2011], the present study has identified a wide range of intra-annual and inter-annual signals from semimonth time series of anomalies over 31 years. The separate analysis for the Atlantic, Indian, and Pacific Oceans minimizes biases from dominating global signals and highlights the regional variability from climate cycles. The clear, multiscale signals from the frequency domain analysis allow examination of any teleconnections across the basins.

The AO is the strongest mode of variability defined by the pressure anomalies in the Northern Hemisphere. The climate cycle has a broad range of frequencies that overshadows other tested indices in the Atlantic. The results show decreasing strength of the AO from north to south as reported by *Bauer* [2001], *Woolf et al*. [2002], and *Dodet et al*. [2010]. Previous studies have focused on the inter-annual variability of the oscillation, but these time scales are only slightly larger than those of a white noise process making the results sensitive to the time period analyzed [*Stephenson et al*., 2000]. The AO index has larger intra-annual variability and the present results demonstrate the importance of the short period oscillations. In the Pacific, the AO has similar

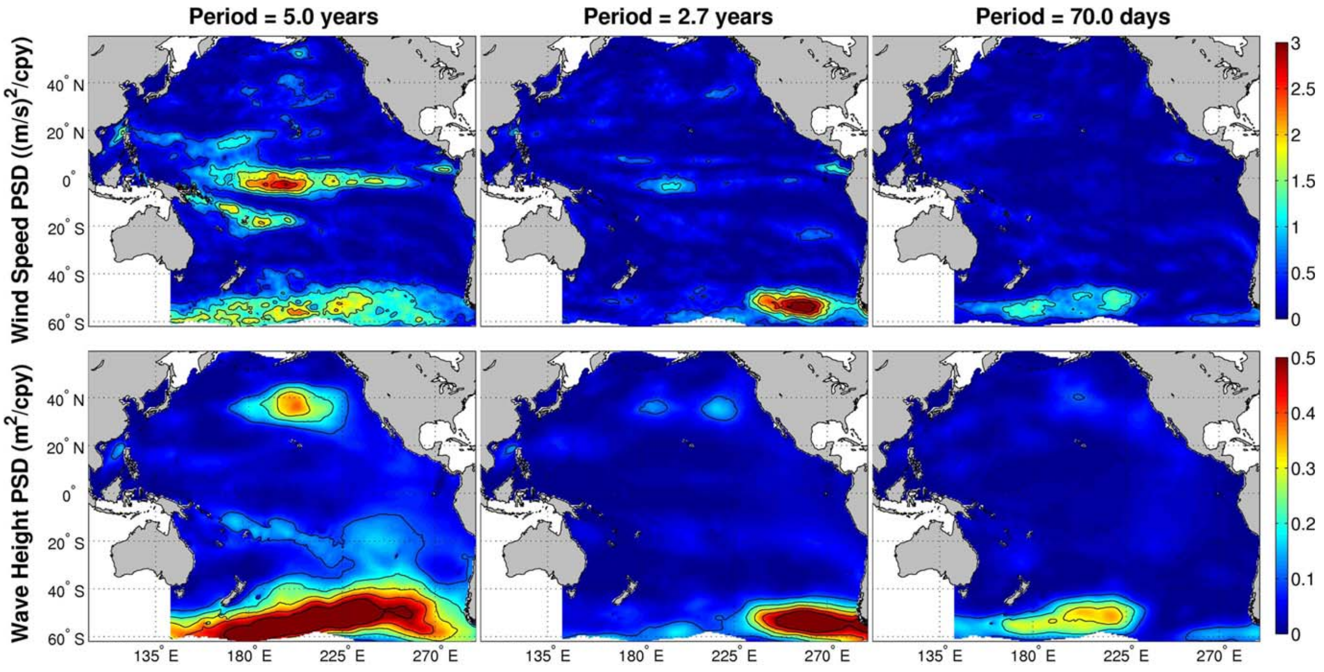
Period = 5.0 years

Period = 2.7 years

Period = 70.0 days

Figure 14. Power spectral density from representative periods for the (top) wind speed and (bottom) significant wave height in the Pacific Ocean.

levels of correlation as in the Atlantic; however, the spatial trimodal pattern is not discernible due to the dominant ENSO signature. The North Pacific Index and Pacific Decadal Oscillation are also known to influence the variations in sea surface temperature and extratropical storms [*Trenberth and Hurrell*, 1994; *Mantua et al*., 1997]. Future studies of the AO can limit the analysis to regions encompassing the Northern Hemisphere or even the North Pacific, where the phenomenon has the strongest signals.

The AAO is equivalently defined from the pressure anomalies in the Southern Hemisphere. The oscillation lacks any significant features in the South Atlantic due to blocking of the east-moving extratropical storms by South America [*Hemer et al*., 2010]. The Indian Ocean shows opposing zonal patterns in the Westerlies with statistically significant correlation with the index. Although the typical AAO structure is not seen in the Pacific basin, the EOFs show a relationship with the index as inferred from the correlation coefficients. The AAO mainly affects the storm belt region of the Westerlies from the Indian to the Pacific Ocean and changes there can have basin-wide effects in the wave field. Through the ERA-40 data set, *Sterl and Caires* [2005] linked the increasing number of storms in the Southern Ocean to increasing trends of significant wave height across the Pacific. *Hemer et al*. [2008] postulated the shift of the Southern Ocean storms has a relationship to the AAO with noticeable impacts on coastal wave measurements near Australia. Modifications in the storm belt directly impact the fetch and subsequently the height and period of the swell in the far field.

The IOD demonstrates its dominance in the Indian Ocean with the largest correlation coefficient in the wind field. The unique and complex wind patterns are located in the equatorial region, where its index is defined, and have teleconnections in the Westerlies. The dominant signals of the wave field are located exclusively in the Westerlies resulting in a stronger relationship to the AAO and ENSO with far-reaching effects. The strong intra-annual components of the winds and waves coincide with the frequency band of the MJO, which has shown its importance near the Equator affecting the rainfall patterns in the Indian Ocean with influences extending into the Pacific and Atlantic [*Wheeler and Hendon*, 2004].

It is well established that the ENSO is triggered in the equatorial Pacific with impacts to the global climate. *Alexander et al*. [2002] shows the lower atmosphere facilitates propagation of the sea surface temperature anomalies to the Indian and Atlantic Oceans. These teleconnections are made possible through the Hadley and Walker cells, which also modify the storm regions of the Westerlies. *Yuan* [2004] uses the “atmospheric bridge” theory to describe the ENSO’s link to the Southern Ocean with distinct impacts to the wind, current, and ice fields. In the Pacific, the ENSO asserts its dominance by obscuring the classic patterns of the AO and AAO. The EOFs best represent its influence on the wind fields in the Nino 3.4 region along the Equator and in the Southern Hemisphere Westerlies. The 5 year spectral component closely resembles the EOFs of the ENSO stressing its importance in the oscillation. The correlation coefficients of the winds and waves show the ENSO plays a role in the Atlantic and Indian Oceans with slightly lower but comparable signals to the AO and IOD, respectively. The analysis here is not sensitive enough to demonstrate the direct impact of the ENSO in the Atlantic and Indian Oceans and more work can be done to identify the teleconnections through the frequency domain analysis.

Figures S1–S12 in the supporting information provide the EOFs, principal components, and spectral density distributions from the ERA-I data set for the three basins. The results allow direct comparisons with Figures 3–14 from CFSR. The two sets of EOFs contain the same dominant climate features corroborated by the principal components. This provides cross verification of the source data, methodology, and findings in this study. The results from CFSR, however, provide better resolution of the general pattern and include fine spatial and temporal features not discernible in ERA-I. The spectral energy distributions of the winds agree reasonably well between the two data sets, but the CFSR wave data produces larger spectral energy than ERA-I. This might be attributed to the better match of CFSR with the upper percentiles and variability of the observations [*Stopa and Cheung*, 2014].

6. Conclusions

The EOF analyses in the time and frequency domains are complementary in detecting the dominant modes of variability in geophysical data sets and provide a consistent and detailed description of climate dynamics. The time domain analysis describes the spatial structure of a phenomenon as it propagates across a basin and evolves through time. The primary EOFs capture the zonal wind structure and the swell propagation in the meridional directions. The results relate the climate information in the CFSR data set to what has been published in the literature and establish a baseline for reference and verification. The analysis in the frequency domain caters to oscillatory signals and provides new information associated with wind and wave climate. The Fourier transform filters out the propagating features to identify the source of climate cycles and elucidate their more subtle patterns by frequency. The EOFs show coherent structures of the climate dynamics in both the time and frequency domains. The higher modes represent intensity and spatial variations of the primary features. The principal components from the EOF analysis reveal the frequency distribution to objectively identify the dominant components associated with the climate cycles in each ocean basin.

The Atlantic Ocean is dominated by regional effects from the north with a broad frequency band and prevailing intra-annual signals of 100–300 days. This corroborates the observed volatility of the North Atlantic climate as all frequencies play a role in its variations. The 100–300 day band exhibits the spatial patterns of the AO. The inter-annual oscillation of 2.5 years affects the same region and may represent endemic variations from nonlinear modulation of the intra-annual components. The Indian Ocean is saturated with mixed inter-annual signals of the AAO, IOD, and ENSO despite having distinct oscillations of 50–90 days period. The 2.1 year oscillation is characterized by a continuous feature in the Southern Indian Ocean, while the pattern at 1.6 years period suggests a meridional teleconnection across the center of the basin. The intra-annual cycles of 50 and 86 days coincide with the MJO, which is known to be active near the Equator. In the Pacific Ocean, the ENSO clearly dominates the variability with its inter-annual signals of 2.7 and 5 years period. The signals are strongest in the equatorial region of the winds and in the Westerlies of the waves. The ENSO proves to be a driver of the wave climate since modifications of the winds in the Westerlies have direct influence on the swells across the basin. These inter-annual oscillations show linkage with a 70 day component suggesting interactions across a wide period range.

This study provides a first look at the frequency content of the wind and wave climate. The global climate is highly coupled and the Fourier transform and EOF analysis provide an objective way to capture the spectral components of the complex phenomena. A common theme in all basins is that the intra-annual and inter-annual oscillations have similar spatial signatures and amplitudes. This suggests the frequency components interact at a wide range of scales stressing the importance of resolving them simultaneously. While the parallel analysis of the CFSR and ERA-I data sets supports the methodology and findings of this study, it is not clear whether the intra-annual oscillations provide forcing to or originate from the inter-annual oscillations. The patterns only confirm that they are both important and their interactions have global implications. Furthermore, the method does not estimate statistical errors of the spectral density due to the use of a single spectrum for the entire time series. Segmentation of the time series can provide an ensemble of spectra for error estimation but at the expense of the long period cycles. The frequency domain EOF analysis opens the door for future research, which can better describe the source, frequency content, spatial signature, uncertainty, and nonlinear interactions of the climate cycles.

Acknowledgments
The Department of Energy funded this study through grant DE-FG-08G018180 via the National Marine Renewable Energy Center. Additional support is provided by NOAA grant NA11-NOS0120039 through the Pacific Island Ocean Observing System program. The CFSR wind and wave data sets and the climate indices are assessable through NOAA National Centers for Environmental Prediction and National Climate Prediction Center. We would like to thank the three anonymous reviewers for their comments and suggestions that have greatly improved this paper. SOEST contribution 9094.

References

Alexander, M. A., I. Blade, M. Newman, J. R. Lanzante, N. C. Lau, and J. D. Scott (2002), The atmospheric bridge: The influence of ENSO teleconnections on air-sea interaction over the global oceans, *J. Clim.*, *15*(16), 2205–2231.

Alves, J. H. G. M. (2006), Numerical modeling of ocean swell contributions to the global wind-wave climate, *Ocean Modell.*, *11*(1–2), 98–122.

Arinaga, R. A., and K. F. Cheung (2012), Atlas of global wave energy from 10 years of reanalysis and hindcast data, *Renewable Energy*, *39*(1), 49–64.

Bacon, S., and D. J. T. Carter (1991), Wave climate changes in the north Atlantic and North Sea, *Int. J. Climatol.*, *11*(5), 545–558.

Barnston, A. G., and R. E. Livezey (1987), Classification, seasonality, and persistence of low-frequency atmospheric circulation patterns, *Mon. Weather Rev.*, *115*(6), 1083–1126.

Bauer, E. (2001), Interannual changes of the ocean wave variability in the North Atlantic and in the North Sea, *Clim. Res.*, *18*(1), 63–69.

Bosserelle, C., C. Pattiaratchi, and I. Haigh (2011), Inter-annual variability and longer-term changes in the wave climate of Western Australia between 1970 and 2009, *Ocean Dyn.*, *61*(1), 63–76.

Bromirski, P. D., D. R. Cayan, and R. E. Flick (2005), Wave spectral energy variability in the northeast Pacific, *J. Geophys. Res.*, *110*, C03005, doi:10.1029/2004JC002398.

Bromirski, P. D., D. R. Cayan, J. Helly, and P. Whittmann (2013), Wave power variability and trends across the North Pacific, *J. Geophys. Res.*, *118*, 6329–6348, doi:10.1002/2013JC009189.

Carvalho, L. M. V., C. Jones, and T. Ambrizzi (2005), Opposite phases of the Antarctic oscillation and relationships with intraseasonal to interannual activity in the tropics during Austral summer, *J. Clim.*, *18*(5), 702–718.

Chawla, A., and H. L. Tolman (2008), Obstruction grids for spectral wave models, *Ocean Modell.*, *22*(1), 12–25.

Chawla, A., D. M. Spindler, and H. L. Tolman (2013), Validation of a thirty year reanalysis using climate forecast system reanalysis winds, *Ocean Modell.*, *70*, 189–206.

Chen, G., B. Chapron, R. Ezraty, and D. Vandemark (2002), A global view of swell and wind sea climate in the ocean by satellite altimeter and scatterometer, *J. Atmos. Oceanic Technol.*, *19*(11), 1849–1859.

Cheung, K. F., Y. Bai, and Y. Yamazaki (2013), Surges around the Hawaiian Islands from the 2011 Tohoku Tsunami, *J. Geophys. Res. Oceans*, *118*, 5703–5719, doi:10.1002/jgrc.20413.

Cox, A. T., and V. R. Swail (2001), A global wave hindcast over the period 1958–1997: Validation and climate assessment, *J. Geophys. Res.*, *106*(C2), 2313–2329.

Dee, D. P., et al. (2011), The ERA-Interim reanalysis: Configuration and performance of the data assimilation system, *Q. J. R. Meteorol. Soc.*, *137*(656), 553–597.

Deser, C. (2000), On the teleconnectivity of the Arctic Oscillation, *Geophys. Res. Lett.*, *27*, 779–782.

Dodet, G., X. Bertin, and R. Taborda (2010), Wave climate variability in the North-East Atlantic Ocean over the last six decades, *Ocean Modell.*, *31*(3–4), 120–131.

Ek, M. B., K. E. Mitchell, Y. Lin, E. Rogers, P. Grunmann, V. Koren, G. Gayno, and J. D. Tarplay (2003), Implementation of Noah land surface model advances in the National Centers for Environmental Prediction operational mesoscale Eta model, *J. Geophys. Res.*, *108*(D22), 8851, doi:10.1029/2002JD003296.

Fan, Y., S.-J. Lin, I. M. Held, Z. Yu, and H. L. Tolman (2012), Global ocean surface wave simulation using a coupled atmosphere-wave model, *J. Clim.*, *25*(18), 6233–6252.

Gemmrich, J., B. Thomas, and R. Bouchard (2011), Observational changes and trends in the northeast Pacific wave records, *Geophys. Res. Lett.*, *38*, L22601, doi:10.1029/2011GL049518.

Gillett, N. P., T. D. Kell, and P. D. Jones (2006), Regional climate impacts of the Southern Annular Mode, *Geophys. Res. Lett.*, *33*, L23704, doi:10.1029/2006GL027721.

Gilman, D. L., F. J. Fublister, and J. M. Mitchell (1963), On the power spectrum of "red noise," *J. Atmos. Sci.*, *20*(2), 182–183.

Graham, N. E., and H. F. Diaz (2001), Evidence for intensification of North Pacific winter cyclones since 1948, *Bull. Am. Meteorol. Soc.*, *82*(9), 1869–1893.

Gulev, S. K., and V. Grigorieva (2006), Variability of the winter wind waves and swell in the North Atlantic and North Pacific as revealed by voluntary observing ship data, *J. Clim.*, *19*(21), 5667–5685.

Gulev, S. K., V. Grigorieva, A. Sterl, and D. Woolf (2003), Assessment of the reliability of wave observations from voluntary observing ships: Insights from the validation of a global wind wave climatology based on voluntary observing ship data, *J. Geophys. Res.*, *108*(C1), 3236, doi:10.1029/2002JC001437.

Hemer, M. A., I. Simmonds, and K. Keay (2008), A classification of wave generation characteristics during large wave events on the Southern Australia margin, *Cont. Shelf Res.*, *28*(4–5), 634–652.

Hemer, M. A., J. A. Church, and J. R. Hunter (2010), Variability and trends in the directional wave climate of the Southern Hemisphere, *Int. J. Climatol.*, *30*(4), 475–491.

Hurrell, J., and C. Deser (2010), North Atlantic climate variability: The role of the North Atlantic oscillation, *J. Mar. Syst.*, *78*(3–4), 231–244.

Izaguirre, C., F. J. Mendez, M. Menendez, and I. J. Losada (2011), Global extreme wave height variability based on satellite data, *Geophys. Res. Lett.*, *38*, L10607, doi:10.1029/2011GL047302.

Jiang, X. W., S. Yang, J. P. Li, Y. Q. Li, H. R. Hu, and Y. Lian (2013), Variability of the Indian Ocean SST and its possible impacts on summer western North Pacific anticyclone in the NCEP Climate Forecast System, *Clim. Dyn.*, *41*(7–8), 2199–2212.

Kalnay, E., et al. (1996), The NCEP/NCAR 40-year reanalysis project, *Bull. Am. Meteorol. Soc.*, *77*(3), 437–471.

Kistler, R., et al. (2001), The NCEP-NCAR 50-year reanalysis: Monthly means CD-ROM and documentation, *Bull. Am. Meteorol. Soc.*, *82*(2), 247–267.

Madden, R. A., and P. R. Julian (1972), Description of global-scale circulation cells in the Tropics with a 40–50 day period, *J. Atmos. Sci.*, *29*(10), 1109–1123.

Mantua, N. J., S. R. Hare, Y. Zhang, J. M. Wallace, and R. C. Francis (1997), A Pacific interdecadal climate oscillation with impacts on salmon production, *Bull. Am. Meteorol. Soc.*, *78*(6), 1069–1079.

Menendez, M., F. J. Mendez, I. J. Losada, and N. E. Graham (2008), Variability of extreme wave heights in the northeast Pacific Ocean based on buoy measurements, *Geophys. Res. Lett.*, *35*, L22607, doi:10.1029/2008GL035394.

Munger, S., and K. F. Cheung (2008), Resonance in Hawaii waters from the 2006 Kuril Islands Tsunami, *Geophys. Res. Lett.*, *35*, L07605, doi:10.1029/2007GL032843.

Neelin, J. D., D. S. Battisti, A. C. Hirst, F. F. Jin, Y. Wakata, T. Yamagata, and S. E. Zebiak (1998), ENSO theory, *J. Geophys. Res.*, *103*(C7), 14,261–14,290.

Pezza, A. B., H. A. Rashid, and I. Simmonds, (2012), Climate links and recent extremes in Antarctic sea ice, high-latitude cyclones, Southern Annular Mode and ENSO, *Clim. Dyn.*, *38*(1–2), 57–73.

Rascle, N., and F. Ardhuin (2013), A global wave parameter database for geophysical applications. Part 2: Model validation with improved source term parameterization, *Ocean Modell.*, *70*, 174–188.

Rayner, N. A., D. E. Parker, E. B. Horton, C. K. Folland, L. V. Alexander, D. P. Rowell, E. C. Kent, and A. Kaplan (2003), Global analyses of sea surface temperature, sea ice, and night marine air temperature since the late nineteenth century, *J. Geophys. Res.*, *108*(D14), 4407, doi:10.1029/2002JD002670.

Roeber, V., Y. Yamazaki, and K. F. Cheung (2010), Resonance and impact of the 2009 Samoa tsunami around Tutuila, American Samoa, *Geophys. Res. Lett.*, *37*, L21604, doi:10.1029/2010GL044419.

Saha, S., et al. (2010), The NCEP Climate Forecast System Reanalysis, *Bull. Am. Meteorol. Soc.*, *91*(8), 1015–1057.

Saji, N. H., B. N. Goswami, P. N. Vinayachandran, and T. Yamagata (1999), A dipole mode in the tropical Indian Ocean, *Nature*, *401*, 360–363.

Semedo, A., K. Suselij, A. Rutgersson, and A. Sterl (2011), A global view on the wind sea and swell climate and variability from ERA-40, *J. Clim.*, *24*(5), 1461–1479.

Shimura, T., N. Mori, and H. Mase (2013), Ocean waves and teleconnection patterns in the northern hemisphere, *J. Clim.*, *26*(21), 8654–8670, doi:10.1175/JCLI-D-12-00397.1.

Smith, T. M., R. W. Reynolds, T. C. Peterson, and J. Lawrimore (2008), Improvements to NOAA's historical merged land-ocean surface temperature analysis (1880–2006), *J. Clim.*, *21*(10), 2283–2296.

Stephenson, D. B., V. Pavan, and R. Bojariu (2000), Is the North Atlantic Oscillation a random walk?, *Int. J. Climatol.*, *20*, 1–18.

Sterl, A., and S. Caires (2005), Climatology, variability and extrema of ocean waves: The web-based KNMI/ERA-40 wave atlas, *Int. J. Climatol.*, *25*(22), 963–977.

Sterl, A., G. J. Komen, and D. Cotton (1998), 15 years of global wave hindcasts using ERA winds: Validating the reanalyzed winds and assessing the wave climate, *J. Geophys. Res.*, *103*(C3), 5477–5492.

Stopa, J. E., and K. F. Cheung (2014), Intercomparison of wind and wave data from the ECMWF Reanalysis Interim and the NCEP Climate Forecast System Reanalysis, *Ocean Modell.*, *75*, 65–83.

Stopa, J. E., K. F. Cheung, H. L. Tolman, and A. Chawla (2013a), Patterns and cycles in the Climate Forecast System Reanalysis wind and wave data, *Ocean Modell.*, *70*, 207–220.

Stopa, J. E., J.-F. Filipot, N. Li, K. F. Cheung, Y.-L. Chen, and L. Vega (2013b), Wave energy resources along the Hawaiian Islands chain, *Renewable Energy*, *55*, 305–321.

Swail, V., and A. Cox (2000), On the use of NCEP/NCAR reanalysis surface marine wind fields for a long-term north Atlantic wave hindcast, *J. Atmos. Oceanic Technol.*, *17*(4), 532–545.

Thompson, D. W. J., and J. M. Wallace (1998), The Arctic Oscillation signature in the wintertime geopotential height and temperature fields, *Geophys. Res. Lett.*, *25*(5), 1297–1300.

Tolman, H. L., and D. V. Chalikov (1996), Source terms in a third-generation wind-wave model, *J. Phys. Oceanogr.*, *26*(11), 2497–2518.

Tolman, H. L., B. Balasubramaniyan, L. D. Burroughs, D. V. Chalikov, Y. Y. Chao, H. S. Chen, and V. M. Gerald (2002), Development and implementation of wind generated ocean surface wave models at NCEP, *Weather Forecasting*, *17*(2), 311–333.

Tolman, H. L., M. L. Banner, and J. M. Kaihatu (2013), The NOPP operational wave model improvement project, *Ocean Modell.*, *70*, 2–10.

Trenberth, K. E. (1984), Signal versus noise in the Southern oscillation, *Mon. Weather Rev.*, *112*(2), 326–332.

Trenberth, K. E., and J. W. Hurrell (1994), Decadal atmosphere-ocean variations in the Pacific, *Clim. Dyn.*, *9*(6), 303–319.

Tsai, C. P., C. H. Hwang, C. Hwa, and H. Y. Cheng (2012), Study on the wave climate variation to the renewable wave energy assessment, *Renewable Energy*, *38*(1), 50–61.

Turner, J. (2004), The El Nino-Southern oscillation and Antarctica, *Int. J. Climatol.*, *24*(1), 1–31.

Ummenhofer, C. C., M. H. England, P. C. McIntosh, G. A. Meyers, M. J. Pook, J. S. Risbey, A. S. Gupta, and A. S. Taschetto (2009), What causes southeast Australia's worst droughts?, *Geophys. Res. Lett.*, *36*, L04706, doi:10.1029/2008GL036801.

Walker, G. T., and E. W. Bliss (1932), World weather V, *Mem. R. Meteorol. Soc.*, *4*(36), 53–83.

Walker, G. T., and E. W. Bliss (1937), World weather VI, *Mem. R. Meteorol. Soc.*, *4*(39), 119–139.

Wang, X. L., and V. R. Swail (2001), Changes of extreme wave heights in Northern Hemisphere Oceans and related atmospheric circulation regimes, *J. Clim.*, *14*(10), 2204–2221.

Wang, X. L., V. R. Swail, and F. W. Zwiers (2006), Climatology and changes of extratropical cyclone activity: Comparison of ERA-40 with NCEP/NCAR reanalysis for 1958–2001, *J. Clim.*, *19*, 3145–3166, doi:10.1175/JCLI3781.1.

Wheeler, M., and H. Hendon (2004), An all-season real-time multivariate MJO index: Development of an index for monitoring and prediction, *Mon. Weather Rev.*, *132*(8), 1917–1932.

Woolf, D. K., P. G. Challenor, and P. D. Cotton (2002), Variability and predictability of the North Atlantic wave climate, *J. Geophys. Res.*, *107*(C10), 3145, doi:10.1029/2001JC001124.

Yang, F., H. L. Pan, S. K. Krueger, S. Moorthi, and S. J. Lord (2006), Evaluation of the NCEP Global Forecast System at the ARM SGP Site, *Mon. Weather Rev.*, *134*(12), 3668–3690.

Young, I. R. (1999), Seasonal variability of the global ocean wind and wave climate, *Int. J. Climatol.*, *19*(9), 931–950.

Young, I. R., S. Zieger, and A. V. Babanin (2011), Global trends in wind speed and wave height, *Science*, *332*(6028), 451–455.

Yuan, X. (2004), ENSO-related impacts on Antarctic sea ice: A synthesis of phenomenon and mechanisms, *Antarct. Sci.*, *16*(4), 415–425.